



# Hyperspectral image segmentation: a comprehensive survey

Reaya Grewal<sup>1</sup> · Singara Singh Kasana<sup>1</sup> · Geeta Kasana<sup>1</sup>

Received: 8 September 2021 / Revised: 29 June 2022 / Accepted: 13 September 2022 /

Published online: 29 October 2022

© The Author(s), under exclusive licence to Springer Science+Business Media, LLC, part of Springer Nature 2022

## Abstract

Hyperspectral Images, which are high-dimensional in nature and capture bands over hundreds of wavelengths of the electromagnetic spectrum. These images have piqued researchers' curiosity in the last two decades. The purpose of this paper is to investigate how researchers segmented and classified Hyperspectral Images with unbalanced data and few labelled training examples. For the sake of comprehension, the background of Hyperspectral Images and segmentation techniques is briefly discussed at first. The study is organised around different Hyperspectral Image processing techniques such as thresholding, clustering, watershed, deep learning, and other methods. The recent trends and developments in HSI segmentation have been reviewed and compiled using benchmark datasets such as Indian Pines, Salinas Valley, Pavia University, and others. Finally, it is intended that the readers will gain a thorough understanding of existing segmentation techniques, their performance, and fresh research areas for HSI that need to be studied or explored.

**Keywords** Hyperspectral images · Segmentation · Thresholding · Clustering · Superpixels · Edge detection · Region growing and merging · Watershed · Classification · Deep learning

## 1 Introduction

With advancements in imaging technology, images with high spatial and spectral resolution have been obtained. The spectrum is divided into numerous bands in HyperSpectral Images (HSI), and a lot of information can be obtained in a great number of wavelengths other than visible light. The details are captured by the HSI sensors as ‘images’ of narrow wavelength

---

✉ Singara Singh Kasana  
singara@thapar.edu

Reaya Grewal  
rgrewal\_phd19@thapar.edu

Geeta Kasana  
gkasana@thapar.edu

<sup>1</sup> Computer Science and Engineering Department, Thapar Institute of Engineering and Technology Patiala, Punjab, India

regions called as spectral bands which are combined to generate a 3-D ( $x, y, \lambda$ ) hypercube that is used for processing, where ‘ $x$ ’ and ‘ $y$ ’ represent spatial dimensions and ‘ $\lambda$ ’ represents spectral dimension (i.e. a range of wavelengths). The spectral and spatial conceptual views are shown in Fig. 1.

The potential applications of HSI analysis are briefly outlined below:

- **Environmental Monitoring** - Researchers have begun major efforts to monitor environmental issues using a variety of applications. For example, [19], tracked air pollution by measuring PM2.5 and PM10 concentrations, while [102] tracked water quality measures.
- **Remote Sensing** - HSI has been widely utilised for land cover classification, detecting changes in land cover that aid in urban planning, detecting roadways [56] and many other applications..
- **Precision Agriculture** - With the benefits of capturing image across multiple bands, The chemical qualities of fruits and vegetables may be examined. For example, as stated later in the study, HSI segmentation has assisted in the detection of deterioration in potatoes, apples, oranges, and peanut kernels. Similarly, HSI images are substantially superior than RGB images for measuring nutrients in soil and diagnosing plant illnesses.
- **Medical Imaging** - Extensive research on the contribution of HSI employing optical characteristics of tissues is being done for non-invasive and effective diagnostic procedures. Cancer cell detection, diabetic, foot ulcer assessment, blood perfusion and oxygenation [27] are just a few examples.

Every scene object leaves a spectral signature, which is a unique fingerprint. As demonstrated in Fig. 1, it assists in the identification of distinct objects by providing the reflection or absorption values of each object or image pixel corresponding to various wavelengths.

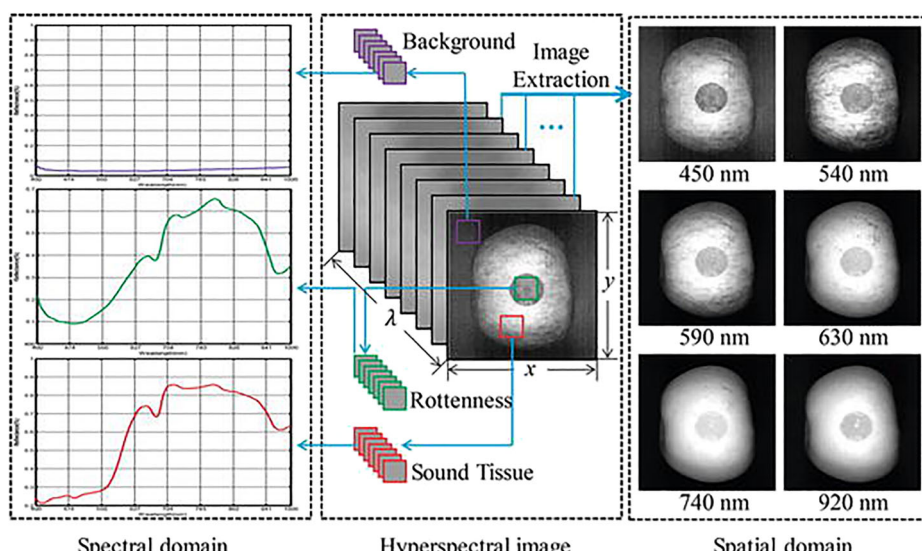


**Fig. 1** Conceptual view of spectral and spatial domain of HSI [49]

RGB images may focus solely on detecting objects or diseases, whereas HSI holds the ability to diagnose the root cause. HSI is being studied extensively for the detection of many objects, materials, and processes. The main difference between RGB and HSI is the number of bands. All three channels can be utilised simultaneously to form segments in RGB images, or their grayscale/binary equivalents can be used easily for segmentation. Segmentation of HSI is very complex due to complexity involved. Researchers have been working on effective segmentation while coping with such high dimensions and few samples in the HSI, which comprises of hundreds of bands for each pixel.

Several cutting-edge methodologies have been used to acquire a better understanding and study of HSI. To make class identification easier and more accurate, researchers have used a variety of pre-processing approaches. For better HSI analysis and classification, the peers are constantly working on image improvement, noise removal, and object extraction.. Segmentation is one of the commonly employed techniques for the same whose benefits have been highlighted in Fig. 2.

Even though there is high spectral resolution, there are lot of spatial distortions, that generates a lot of noise in the HSI. To remove such noise, reduce confusion around boundaries and extract useful information, segmentation plays a vital role. When the images are broken down into desired objects/segments, then the classification of these segments into particular classes can be done more accurately. With the help of various segmentation techniques, the authors have divided the images into various Regions Of Interest(ROI) that exhibit similar properties. These similar properties can have similar spectral behaviour, nearest neighbours in spatial context and non-redundant features that give meaningful data. Hence, once the classifier gets to deal with image segments rather than raw pixels, the many(different) objects in an image can be represented effectively. According to previous work, some researchers have solely used spectral information of every pixel and categorized them. This, however, is not very effective method. With the HSI technology, spectral and spatial distortions occur. Same objects having slightly different spectral values tend to

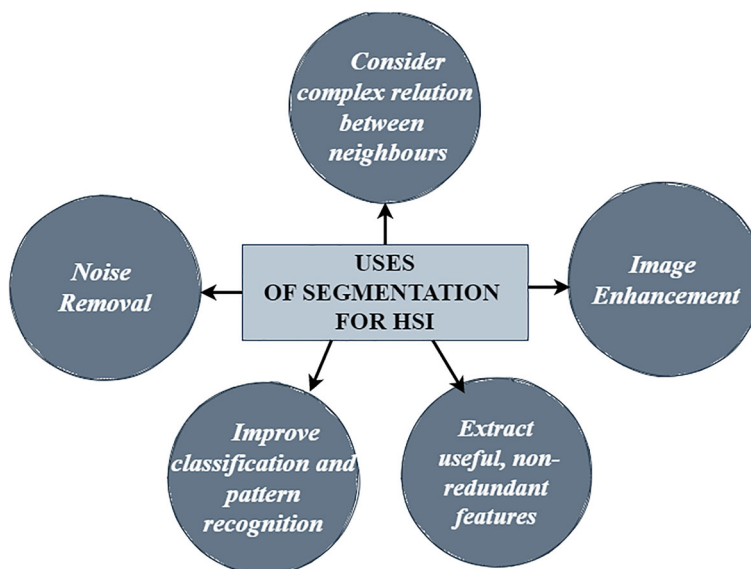


**Fig. 2** Benefits of segmentation in HSI

get differentiated in different classes, whereas, sometimes different objects having similar spectral values tend to get grouped together in same class. As a result, focusing solely on each pixel's spectral vector results in misclassification.

Researchers employed both spectral and spatial information to solve this challenge and enhance segmentation. The neighbourhood information of each pixel, as well as spectral data, were combined in a variety of ways to improve the findings. Morphological, edge detection operators, and watershed segmentation approaches all make good use of picture topological and structural information. Some researchers got segmentation findings at various scales and fused them together to generate a better classification map in order to achieve textural and minute details in images.

With increasing trend of deep learning in computer vision, peers have extracted spectral spatial features automatically and produced high quality segments for classification.

Figure 3 generalises the importance of segmentation aided classification of a remotely sensed HSI. Due to atmospheric disturbances, the complex HSI suffers from noisy capture, poorly defined boundaries, imbalanced data, and a great deal of confusion. This example exemplifies the advantages of segmentation-assisted categorization.

The papers reviewed are focused on how different state of the art segmentation techniques have been used for HSI in the previous decade. The peers have worked with unbalanced, lesser, unlabelled training samples and Curse of Dimensionality. Various learners like Support Vector Machine(SVM), Random Forest (RF) and others were used

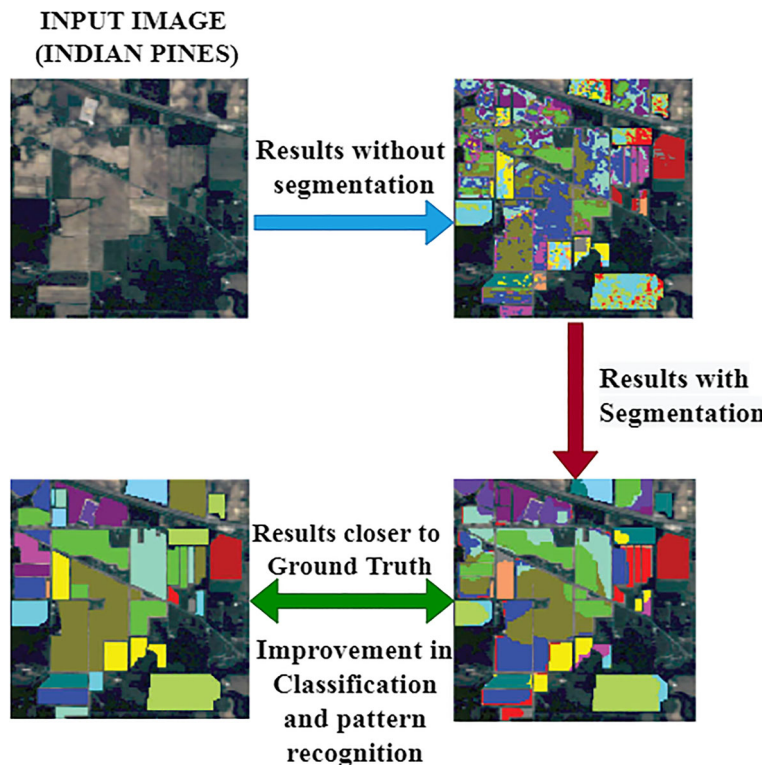


**Fig. 3** Conceptual view on improvement using segmentation

alongwith. The performances of work done by authors was checked using various evaluation parameters like Overall Accuracy, Average Accuracy, Adjusted Rand Index, Peak Signal-to-Noise Ratio and many more. The most recent work in HSI analysis has been thoroughly examined and classified using a variety of segmentation approaches such as thresholding, watershed, clustering, morphological, region based segmentation, deep learning, and superpixels based segmentation.

A brief discussion of existing segmentation methods is done in Section 2. The list of various Evaluation parameters used by peers has also been explained as well. The performance of different techniques on benchmark datasets has been studied. Section 3 has been categorised according to different segmentation methods and the work done by peers using those particular methods. In Section 4, the various segmentation techniques employed by peers have been summarised on the basis of their application and performance. Finally, in Section 5, several conclusions have been drawn based on the articles evaluated, and what can be done in the future to improve HSI segmentation.

## 2 Preliminaries

The available approaches for image segmentation, regularly used assessment parameters, and the benchmark HSI dataset have been briefly described in this section.

### 2.1 Overview of segmentation methods

The classification can be improved and simplified via segmentation. Color, pixel intensity, texture, and a variety of other features all play a part in segmentation. In Fig. 4, various broad segmentation approaches have been highlighted.

- **Thresholding** : It is an intensity based method where pixels belonging to one range of intensity belong to same class and rest of the pixels belong to the other. A threshold decides whether a pixel is an object (intensity value 1) or background (intensity value 0). For a threshold  $T$ ,  $g(x, y) = 1$ , if  $h(x, y) \geq T$  and  $g(x, y) = 0$ , if  $h(x, y) \leq T$  where  $g(x,y)$  and  $h(x,y)$  is output and input image, respectively. Figure 5 shows generalised behaviour of thresholding segmentation.
- **Clustering** : The two most common types of clustering are hierarchical and partitional, which tend to group things together based on their proximity or similarity. Like

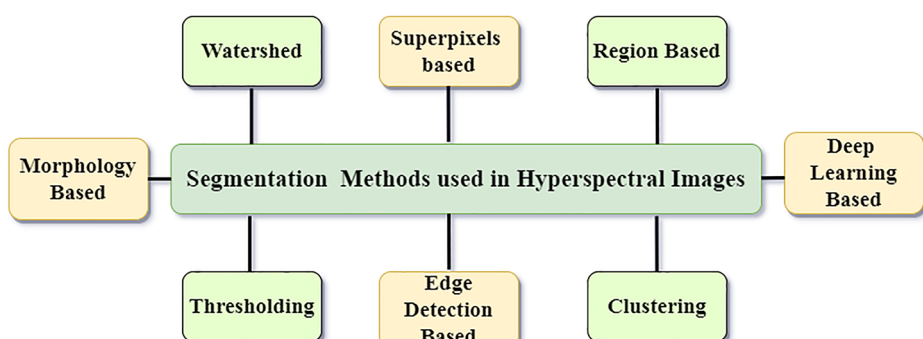


**Fig. 4** General segmentation techniques used in HSI

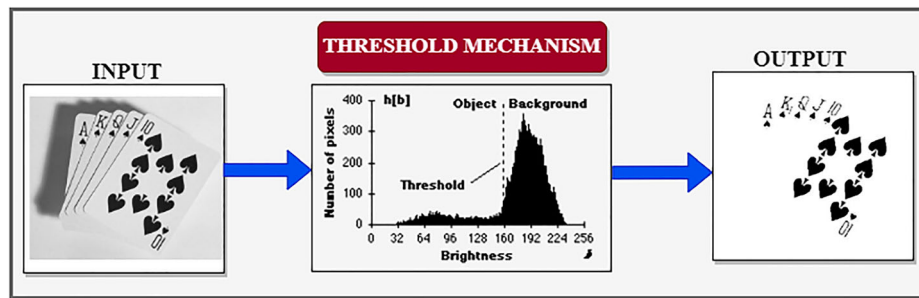


**Fig. 5** Basic threshold segmentation [34]

in k-means clustering, a partitional clustering method, an image is segmented into ‘ $k$ ’ number of predefined clusters, and pixels’ distances are computed with respect to seed points of each cluster, with the shortest distance being the deciding parameter of the pixel to belong in the cluster. As the name implies, hierarchical clustering creates a tree-like hierarchy of clusters. Agglomerative hierarchical clustering is a bottom-up strategy that aggregates individual pixels considered as singletons until a large cluster is formed, whereas divisive hierarchical clustering (top-down approach) segmentation starts with a large cluster and continues until we have singletons. Figure 6 shows generalised behaviour of clustering segmentation.

- **Watershed segmentation** : The gradient of image is treated as a topographic surface where the bright pixels are considered ‘high’ like mountaintops/watershed lines and dark pixels are ‘low’ like valleys/basins. A marker or seed point is taken in each object intuitively, which is then grown using morphological watershed method. The basins are flooded, and regions where floodwater from several basins meets are identified and borders are established using segmentation approach. Figure 7 depicts the fragmentation of watersheds in general.
- **Morphological segmentation** : It entails segmenting images by manipulating their shapes and structure with structural elements. Morphological dilatation fills gaps and holes in images, which increases the boundary size of object. Morphological erosion is the process of removing the outer limit of objects, which results in the removal of minor objects. The result of general morphological procedures on an image is shown in Fig. 8
- **Edge detection based segmentation** : It is based on discontinuity among pixel intensity values and produces binary images. The edges are detected by comparing the first order derivative of the pixels with a particular threshold value or if the second

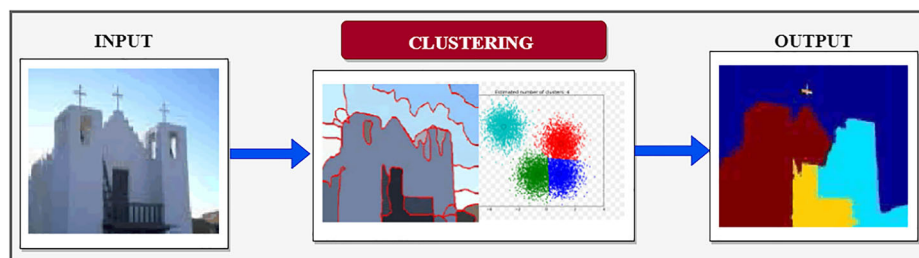


**Fig. 6** Basic clustering segmentation [16]

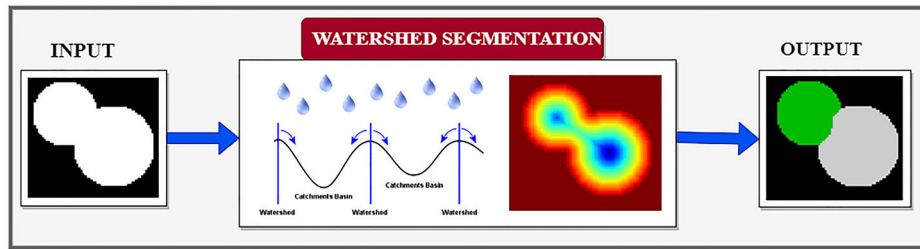


**Fig. 7** Basic watershed segmentation [74]

order derivative have zero crossings. The detected edges are connected to form the object boundaries. Gradient and gray histograms based methods are frequently used and simple edge detection operators like sobel, canny and laplace have also been implemented to segment the image objects. Figure 9 shows generalised edge preserving segmentation.

- **Superpixel segmentation** : Superpixels are groups of pixels with similar characteristics, such as intensity values. These have more information than a single pixel and have a perceptual relevance since comparable pixels have similar visual qualities. The most prevalent approaches for obtaining superpixels are simple linear iterative clustering and entropy rate segmentation. Figure 10 depicts superpixel segmentation in general.
- **Region segmentation** : This approach partitions the regions with comparable properties. This technique is divided into three categories: region growth, region splitting, and region merging. Similar pixels on the basis of grey level, colour, texture, or intensity values are aggregated together with the help of “seed points” to form bigger regions until their similarity is not hindered in region growing, whereas in region splitting and merging, the entire image is treated as a single region that is split further when a specific set of similarity conditions is not met, and then regions are merged, using smaller

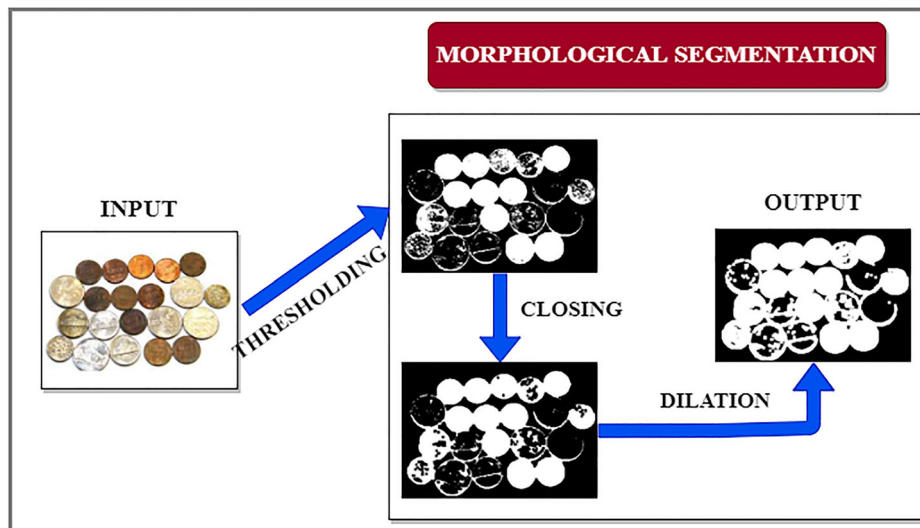


**Fig. 8** Basic morphological segmentation [75]

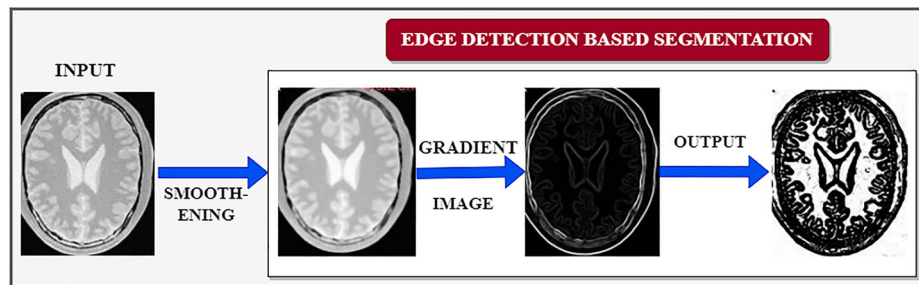


**Fig. 9** Basic edge preserving segmentation [72]

sizes of  $2 \times 2/4 \times 4$  on the basis of homogeneity. Iteratively, both splitting and merging occur. Figure 11 depicts segmentation based on generalised regions.

- **Deep Learning** : It works in the same way as the human brain. Multiple hidden nodes in neural networks aid in obtaining numerous high-level properties that wonderfully segment the images. Figure 12 depicts the generalised behaviour of Deep Learning segmentation.

## 2.2 Methodology adopted for the survey

The aim of the survey is to explore how the state of the art segmentation techniques have been used and performed on Hyperspectral Images.

- The research papers have been reviewed from 2010 onwards till now, from reputed and leading sources like ScienceDirect, IEEE and others.
- Different segmentation approaches were used to organise the paper. Each technique's benefits and drawbacks have been highlighted.
- Land cover benchmark datasets such as Indian Pines, Pavia University, and others have been used to assess the performance of approaches.
- Each technique's performance was presented and compared using the performance parameters listed.

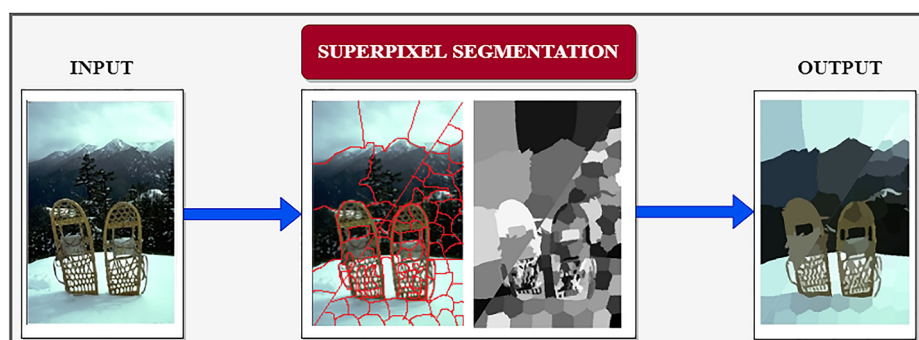


**Fig. 10** Basic superpixel based segmentation [68]

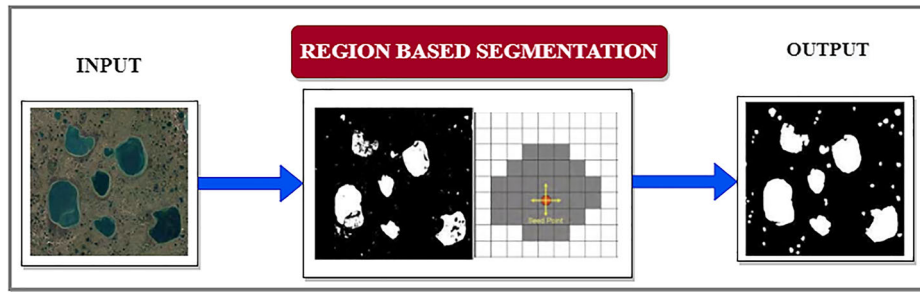


**Fig. 11** Basic region based segmentation [76]

- **Overall Accuracy (OA)** - It measures the percentage of correctly classified samples. It is summation of accurate recognition of samples divided by total number of samples.

$$OA = \frac{\sum_{i=1}^C M_{ii}}{N} \quad (1)$$

where  $C$  is the total number of labels/classes.  $M_{ii}$  represents the samples that actually belonged to  $i$ th class and were predicted to belong to  $i$ th class.

- **Average Accuracy (AA)** - It measures the average percentage of correctly classified samples for an individual class.

$$AA = \frac{(\sum_{i=1}^C (M_{ii} / \sum_{j=1}^C M_{ij}))}{C} \quad (2)$$

where  $C$  is the total number of labels/classes.  $M_{ij}$  represents the samples that actually belonged to  $i$ th class and were predicted to belong to  $j$ th class.

- **Kappa Coefficient (k)** - It measures the percentage agreement corrected by the level of agreement that could be expected by chance alone an class-specific accuracy.

$$k = \frac{(N(\sum_{i=1}^C M_{ii}) - \sum_{i=1}^C (\sum_{j=1}^C M_{ij} \sum_{j=1}^C M_{ji}))}{(N^2 - (\sum_{j=1}^C M_{ij} \sum_{j=1}^C M_{ji}))} \quad (3)$$

where  $C$  is the total number of labels/classes.  $M_{ii}$  represents the samples that actually belonged to  $i$ th class and were predicted to belong to  $i$ th class,  $M_{ij}$  represents the samples that actually belonged to  $i$ th class and were predicted

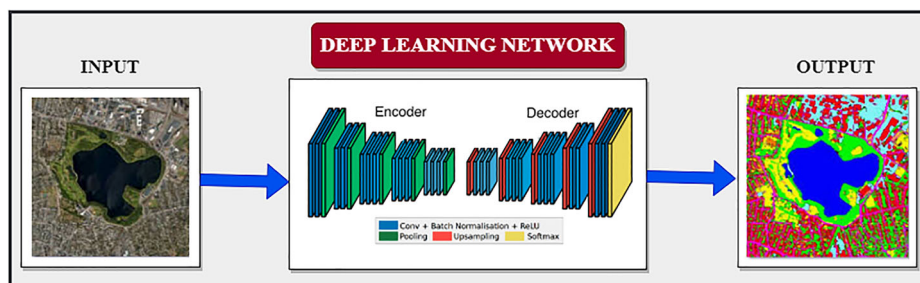


**Fig. 12** General deep learning based segmentation [61]

to belong to  $j$ th class and  $M_{ji}$  represents the samples that actually belonged to  $j$ th class and were predicted to belong to  $i$ th class.

- **Coefficient of Determination ( $R^2$ )** - It is used for regression analysis and check strength of model. It is a statistical measure of dependence between two variables. It measures the variance in response variable  $y$  as predicted by the predictor variable  $x$ . It is written as

$$R^2 = \frac{SSR}{SST} \quad (4)$$

where

$$SSR = \sum_i (\hat{y}_i - \bar{y})^2, SST = \sum_i (y_i - \bar{y})^2 \quad (5)$$

where  $SSR$  is Sum of Squared Regression,  $SST$  is Total variation in the data,  $y_i$  is the value  $y$  for observation  $i$ ,  $\bar{y}$  is mean of  $y$  value and  $\hat{y}$  is the predicted value of  $y$  for observation  $i$ .

- **Root Mean Square Error Of Prediction (RMSEP)** - It is a standard parameter to measure the error of a model in predicting the classes of samples. It expresses how concentrated the data is around the curve of best fit. Mathematically, it is difference between actual and predicted labels of  $N$  samples.

$$RMSEP = \sqrt{\frac{(\sum_{i=1}^N (Predicted_i - Actual_i)^2)}{N}} \quad (6)$$

- **Adjusted Rand Index (AR) and Davis-Bouldin Index (DB)** - The efficiency of the clustering algorithms can be evaluated using AR and DB indexes. AR is the agreement between two partitions. It measures the similarity between the proposed clustering algorithm and the ground truth. Higher the AR index, better are the results. DB index measures the validation of the clustering of how well it has been performed with respect to the inherent features of the dataset. It is the ratio of intra-cluster scatter and inter-cluster distance. Lower the value of DB index, better is the performance.
- **Peak Signal-to-Noise ratio (PSNR)** - It is an image quality metric. It is the ratio between the maximum possible value (power) of the signal (ideal image) and power of the noise. For a standard image,

$$PSNR = 20 \log_{10} \left( \frac{L - 1}{MSE} \right) \quad (7)$$

where  $L$  is the maximum number of intensity levels,  $O$  is the original image,  $D$  is the degraded image,  $m$  is number of pixels in a row,  $n$  is number of pixels in a column,  $i$  is index of row in the image and  $j$  is the index of column in the image.

$$MSE = \frac{1}{mn \sum_{i=0}^{m-1} \sum_{j=0}^{n-1} (O(i, j) - D(i, j))^2} \quad (8)$$

- **Jaccard Index** - It is a statistical measure used for classification and segmentation to find similarity and diversity among data samples. It is the area of overlap over area of union. For two sets  $A$  and  $B$ , it is represented as

$$J(A, B) = \frac{(A \cap B)}{(A \cup B)} \quad (9)$$

- **Normalised Mutual Information (NMI)** - Mutual Information (MI) evaluates the quality of clustering by comparing the data clusters with classification labels. It tells how much both agree with each other or how much information is shared. A lower  $MI$  value indicates that there is no correlation between the two, implying that the cluster produced is inaccurate. NMI is bias corrected and normalises the value between 0 and 1. Mathematically,

$$NMI(X, C) = \frac{2 \times I(X; C)}{[H(X) + H(C)]} \quad (10)$$

where  $X$  is the cluster label,  $C$  is the class label,  $H(\cdot)$  is the entropy and  $I(X; C)$  is the MI between  $X$  and  $C$  and

$$I(X; C) = H(X) - H(X/C) \quad (11)$$

where  $H(X/C)$  is the entropy of class labels within each cluster.

- **Global Consistency Error (GCE)** - GCE measures the level to which one segmentation can be seen as a refinement of other segmentation result. The two segmentation results that are consistent have less or zero GCE. If one segment is proper subset of another segment, then it is a refinement. If no subset relationship is found, then the overlapping regions are considered to be inconsistent.

$$GCE = (1/n) \times \min \sum_i E(S1, S2, pix), \sum_i E(S2, S1, pix) \quad (12)$$

where  $S1$  and  $S2$  are two segmentations as input,  $pix$  is the pixel value and the output is in range [0,1]. 0 signifies no error.

- **Receiver Operating Characteristic Curve (ROC) and Area Under Curve (AUC)** - ROC graph shows the performance of a classification model at different classification thresholds. It is a trade-off between True Positive Rate (TPR) and False Positive Rate (FPR). A good performance of model is the one having cut-off with highest TPR and lowest FPR. AUC is the area under ROC curve whose value lies between [0.5 and 1]. It gives combined performance of a model under all the classification thresholds. Higher the AUC, better the model is in classification.

- After investing in the performance of various techniques, the direction for the community of researchers is discussed in the end.

### 2.3 Benchmark HSI datasets

The following are some of the most widely utilised datasets by peers for segmentation and HSI analysis.

- **Indian Pines (IP)** : This image was captured by AVIRIS sensor over Indian Pines site. It has 224 spectral bands and  $145 \times 145$  pixels. The scene contains 16 classes, majorly consisting of agricultural land, forest and vegetation. It also contains highways, roads, low density housing and man made built structures.
- **Pavia University (PU) and Centre** : These scenes were captured by ROSIS sensor over Pavia in Northern Italy. The centre has 102 bands whereas University contains 103 bands. The 9 classes majorly contain water, trees, soil and man built structures.
- **Salinas Valley (Sa)** : This scene was captured by AVIRIS sensor in California. It has 224 spectral bands and 16 classes. It includes vineyards, soil and vegetables.

- **Kennedy Space Center (KSC)** : The NASA AVIRIS sensor captured the scene in Florida having 13 classes. It majorly consists of vegetation and water.
- **Botswana (Bo)** : The scene was captured in Delta, Botswana containing 14 classes and 242 bands. It had majorly swamps and woodlands.

### 3 Existing segmentation techniques used for HSI

Different segmentation approaches covered in previous sections are grouped in this section, and relevant publications are reviewed.

#### 3.1 Threshold based methods

To reach n-level thresholds, [31] used Fractional-Order Darwinian Particle Swarm Optimization (FODPSO) on segmented coloured images. It solves the local optimum problem of previous evolutionary algorithms as well as the Otsu method's fixed threshold problem. The authors [32] extended FODPSO to optimise multilevel thresholding on HSI, inspired by the aforementioned approach. When the object of interest did not appear as a peak in the histogram, it suffered from inhomogeneity and was unable to segment well. After FODPSO, the authors used Mean Shift Segmentation (MSS) with two distinct kernel sizes to solve this problem. On the Pavia Centre and Salinas Valley datasets, SVM classification was employed and high OA was attained.

Thresholding was used to segment bruises on apples by [17]. Raw images were compressed by Principal Component Analysis (PCA) to remove redundant information from the HSI cubes. Thresholding helped in creating the binary mask that removed background. Region Of Interests (ROIs) were selected manually afterwards. Various models like Decision Tree (DT), Support Vector Machine (SVM), gradient tree boosting and Random Forests (RF) were applied on a dataset of 60 apples' images captured using Surface Optics Corporation, SOC710 camera having 128 bands. RF achieved the highest accuracy of 99.90% as compared to other models. It also performed better than basic image processing method - Otsu Threshholding.

The eight different cloth materials, segmented by [33] and recognised Gunshot Residue (GSR) patterns. There were two types of anomaly detection situations considered: unsupervised and supervised. The GSR particles were extracted in an unsupervised setting using the Reed Xialo (RX) anomaly detection technique. To assess if a pixel was anomalous or not, the data was modelled as multivariate Gaussian and the RX score was produced using sample mean, variance, and threshold. GSR and background were supervised classified using SVM. Surface Optics SOC710-VP hyperspectral camera with 128 bands was used to capture the images. The overall accuracy ranged between 74.5% and 100%.

To determine protein content in peanuts, [94] used the spectral information of ROIs. ROIs were segmented using thresholding where a mask was formed at manual threshold value of 0.225. The authors measured protein content using Kjeldahl method also for reference. The covariance between spectral data of the HSI and reference measured protein contents built the Partial Least Squares Regression (PLSR) calibration model. The regression coefficients shortlisted eight useful and most informative wavelengths. With PLSR, Coefficient Of Determination (COD) of 0.885 and Root Mean Square Error of Prediction (RMSEP) of 0.465% was recorded. These parameters obtained values 0.870 and 0.494%, respectively using eight effective wavelengths.

Ye et al. [93] detected and graded bruises on potato. Whole potato served as ROI and segmented from the background using binary mask by setting a manual threshold value of 255. To reduce signal to noise ratio, Savitzky-Golay (SG), first derivative, second derivative and Standard Normal Variate were applied. SVM classification was used whose modeling parameters were optimized using grid search algorithm. These steps achieved an accuracy of 90.63%. The authors also removed redundant features using Simulated Annealing Algorithm (SNA) which increased the accuracy to 96.88%

The different approaches of thresholding used by peers for HSI segmentation are shown in Fig. 13.

Wu et al. [91] presented an adaptive threshold segmentation method to tackle the problem of manual empirical value selection. The threshold was calculated using the mean value of the distances between the training samples and the spectral center of each class. The Euclidean distance between pixels was employed as constraint and compared with this threshold. K-Nearest Neighbours (KNN) algorithm was used over the segmented region for classification. The steps carried out are briefly depicted in Fig. 14. The overall methodology was applied on 10% and 2% training samples of each class of Indian Pines and Pavia University dataset, respectively. The former dataset achieved an OA and kappa of 95.13% and 0.9444, respectively. The latter dataset achieved an overall accuracy and kappa of 95.52% and 0.9416, respectively. When training samples were dispersed far from the border, the proposed work lacked an efficient constraint ability for segmentation. This resulted in a classification map with a mixed distribution. Texture information embedded in the code could help in the production of better results.

Noviyanto and Abdulla [65] employed thresholding to separate honey samples from the background in a container. When the position of honey samples was static, manual segmentation was used. This aided in the creation of the model. Honey locations were dynamic and unknown in the testing setting, hence automatic segmentation was used. The authors used a circular hough transform at 439.41 nm to achieve a high contrast between the honey containers and the background. The round honey jars were identified, and grid-based segmentation was carried out.

Tian et al. [81] suggested a multi-region model based on brightness grade segmentation to estimate Soluble Solids Content (SSC) in apples. The spectra of the core, middle, and outside regions were collected using hyperspectral reflectance imaging. Along with standard PLS and Multi-region Average PLS, a Multi-region Combined Partial Least Square

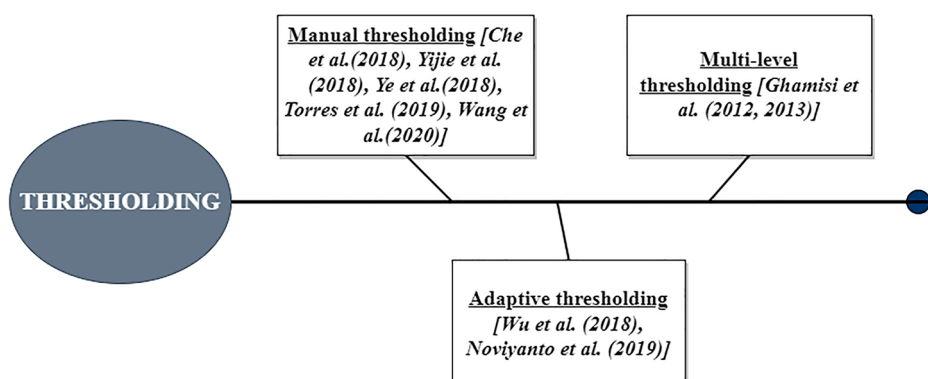


**Fig. 13** Different methods of thresholding in survey

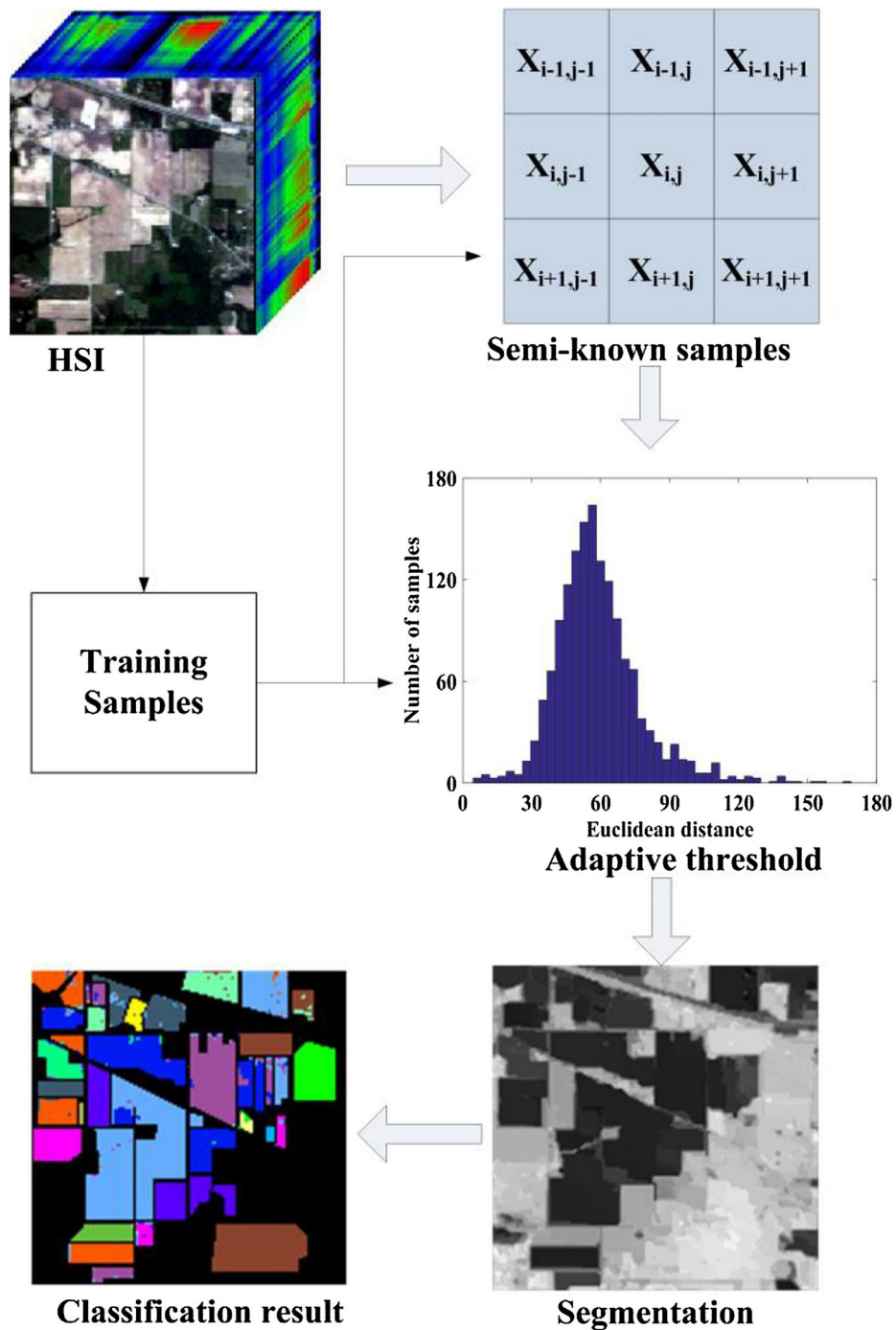


**Fig. 14** Methodology steps [91]

(MCPLS) model of SSC was developed (MAPLS). A binary mask with a threshold value of 20 at 710 nm removed background. When compared to standard PLS and MAPLS, MCPLS produced better outcomes.

With thresholding, [82] separated green oranges from leaves. From the Visible Near-Infrared (VIS-NIR) and Short Wave Infrared (SWIR) areas, relevant bands were recovered using Analysis Of Variance (ANOVA) and PCA. A manual threshold was set for segmentation, and a band ratio was used to choose more discriminative bands. ANOVA and PCA were used to derive this band ratio from two different wavelengths. In the VIS-NIR region, 96.97 percent of the pixels were correctly identified to distinguish between green oranges and leaves, but in the SWIR region, only 74.79 percent of the pixels were correctly classified to distinguish between green oranges and leaves. For defects detection, 92.93% and 89.31% of the pixels were classified correctly in VIS-NIR and SWIR region, respectively.

Zhou et al. [105] used threshold segmentation to predict seed germination states. The wavelength was chosen to provide a high contrast between the seeds and the background. The image was divided into a single seed image, and the seed's mask was constructed with the help of filtering and dilation. SVM, RF, and Light Gradient Boosting Machine (LightGBM) models were used to classify the wavelengths that had a higher information gain than a threshold. The prediction accuracy of the LightGBM model was found to be the best at 89 %.

Potassium (K) and phosphorus (P) contents were monitored by [90]. The leaves were segmented from the background using single band grayscale image at 1095nm. The authors used manual threshold value of 0.15 to create binary mask of leaf. SNV was used to remove noise interference and dimension was reduced using SPA. For prediction, Regression Coefficient (RC) of PLSR model were used. SPA- Multiple linear regression (MLR) yielded best performance of Coefficient Of Prediction (COD) of 0.9423 (P) and 0.9168 (K).

Das et al. [25] focused on generating HSI Attribute Profiles (APs) by selecting thresholds. If the attribute value of related components was less than a threshold, APs connected them and merged them with background. The thresholds were chosen based on the image's max-tree and min-tree representations, which captured sufficient spatial information. Filtered images were made and combined with the source image to create APs using these thresholds. It produced low-dimensional, non-redundant, and computationally efficient profiles. On the attribute Diagonal of Bounding Box, it received the maximum OA of 95.86% for Indian Pines dataset (DBB).

Liu et al. [55] used a convolutional neural network and threshold segmentation to identify mouldy peanut kernels. To label the peanuts as mouldy, healthy, or damaged, and to identify the backdrop, manual threshold values were used. For classification, Deeplab v3, Segnet, Unet, and Hypernet deep models were used. The authors improved the performance of these models by 0.43-4.96 % by using Peanut Recognition Index feature pre-extraction (PRI). The comparative analysis of various Threshold segmentation techniques has been discussed in Table 1.

### 3.2 Clustering based segmentation

Chen and Chen [20] used multiple kernel fuzzy c-means clustering to segment the images. The linear combination of kernels was employed, and the linear coefficients of the composite kernels were updated using a derivation of rules. This allowed for the better segmentation of brain MR images by combining diverse pixel information. The method could be applied to more heterogeneous data, such as remote sensing photos, for robust clustering, as mentioned previously.

**Table 1** Comparison analysis of thresholding

Authors	Methodology used	Evaluation parameters
Ghamisi et al. [31]	N-Level thresholding, FODPSO	NA
Ghamisi et al. [32]	Multi-level thresholding, FODPSO, MSS, SVM.	• For PU = OA of 98.04% and k=0.97 • For Sa = OA of 99.13% and k=0.99
Che et al. [17]	Fixed Thresholding to create binary mask, manual ROI selection, PCA, Decision tree, SVM, Gradient tree boosting, RF.	Highest Accuracy of Random Forest $\approx$ 99.90%
Glomb et al. [33]	Reed Xialo anomaly detection, SVM classification	Overall accuracy between 74.5% and 90% for different fabrics.
Yijie and Cheng [94]	Manual threshold value of 0.225 on the grayscale image, PLSR model.	• COD value of 0.885 and RMSEP value of 0.465 • With eight effective wavelengths, COD value of 0.870 and RMSEP value of 0.494
Ye et al. [93]	Manual thresholding, SNA, SVM.	• OA of 90.63% • With SNA, OA increased to 96.88%
Wu et al. [91]	Adaptive thresholding, KNN	• For IP : OA= 95.13% and k= 0.9444. • For PU : OA= 95.52% and k= 0.9416.
Noviyanto and Abdull [65]	Manual and adaptive segmentation, Manual Threshold at wavelength 439.41 nm	NA
Tian et al. [81]	Brightness grade segmentation, binary mask at wavelength 710 nm with threshold value 20, MCPLS prediction model.	The correlation coefficient, RMSEP and residual predictive deviation were 0.9132, 0.3929 and 2.1652 respectively.
Torres et al. [82]	Relevant band selection using ANOVA and PCA, manual thresholding.	• In VSIR, OA of 96.97% for correct distinction between green oranges and leaves. OA of 92.93% for defect detection. • In SWIR, OA of 74.79% for correct distinction between green oranges and leaves. OA of 89.31% for defect detection.
Zhou et al. [105]	Threshold, filtering and dilation, SVM, RF and LightGBM classification.	Accuracy of 89% of LightGBM model using SD2 pre-treatment.
Wang et al. [90]	Manual thresholding value 0.15 at single band wavelength at 1095nm, SNV, SPA, RC, PLSR and MLR.	SPA-MLR achieved highest COP of 0.9423 (P) and 0.9168 (K).
Das et al. [25]	Min-tree and Max-tree for threshold selection	OA of 95.86% on IP.
Liu et al. [55]	Manual Threshold	Highest OA of 99.1 for detection of moldy kernels.

Pisani et al. [69] suggested a land cover categorization approach based on graph partitions called Optimum path forest (OPF). Data nodes, i.e. samples' feature vectors, were used to create OPF. To create ideal path trees for clustering, the authors defined an adjacency connection between nodes and a path-cost function. The graph's arc was weighted by the Euclidean distance between nodes. The weights of the nodes were calculated using a probability density function (pdf) to determine the densities of data samples. To develop OPF, the

nodes with the highest density formed root nodes. Landsat-5, Geoeye, Ikonos-2 MS, and CBERS-2B satellites provided controlled and unsupervised scenarios for the project. The clustering findings were similar, and the supervised OPF beat the supervised classifiers.

Verma et al. [86] applied improved intuitionistic fuzzy c-means clustering for hyperspectral brain picture segmentation. When compared to [20] fuzzy c-means clustering, it produced better results. It comprised each pixel's local spatial information, kept visual features, and was noise resistant.

Projected clustering with region merging was used by [59]. The goal of projected cluster algorithms was to find subspace clusters. Using spectral similarity and spatial adjacency, the data was grouped in spectral/features space and regions were merged in spatial/image space. To combine clusters in picture space, a 2D cluster map was employed. The segmentation map was created from the cluster map using Connected Component Labeling (CCL). Spatially related clusters were given the same label, while spatially disconnected clusters were generated as a new region, even if the cluster label was the same. Projected Energy was used to extract region adjacency data from a segmentation map (PE). PE's global minimum value was combined into a pair of areas. The method was used in the Salinas Valley, Pavia University, and Pavia Center dataset. The methodology outperformed existing clustering methods in terms of purity and Normalized Mutual Information (NMI). The algorithm's flaws included human parameter selection, redundant information in decreased bands, and a long run time.

Mehta and Dikshit [60] improved their segmentation findings using Mutual Nearest Neighbours to remove redundancy in bands (MNN). A local band selection strategy was used, which was based on the bands' redundancy and relevancy values. The k-means technique was initially used to generate segmentation maps. Using MNN information, these maps were combined into clusters to generate a cluster map. The k most significant clusters were chosen using an entropy-based approach. The proposed methodology was tested in the central Spanish La Mancha region, Pavia University, the Salinas Valley, Pavia Center, and the Washington Mall DC. The work exceeded its peers and had the best overall accuracy. The manual selection of settings proved a stumbling block.

For HSI segmentation, [51] used Hierarchical Cluster Analysis (HCA) and K-means Cluster Analysis (KMCA). The images were taken from healthy mice's cutaneous (skin) tissues. KMCA used minimal distances between centroids and pixels to update random initial cluster centres iteratively. Color codes were assigned to spectral clusters in HCA based on spectral similarity. The authors used Euclidean distance to compare spectra and group comparable things together. Following that, distances between new clusters were calculated and blended into a comparable cluster until only one remained. The structures of skin were clearly seen when the number of clusters for both techniques was increased. In comparison to KMCA, HCA fared better in segmenting distinct skin tissues.

Torti et al. [83] used several parallel architectures to improve computing complexity when doing K-means clustering for brain cancer cell identification. The authors used the CUDA, OpenMP, and OpenCL paradigms in their research. K centroids, minimum threshold, and maximum iterations to compute distances and build clusters were all pre-defined in all of these paradigms. In OpenMP, two alternative versions of parallel k-means were created. In the original version, the 'for' loop that traversed the pixels was parallelized. In the meantime, in the second version, iterations and threshold computations were kept serial while the majority of the other code was parallelized. Authors used thousands of parallel threads in CUDA, and three variants of parallel k-means were constructed in this study. In the initial version, distance computation was parallelized. The GPU was used to do error

evaluation (threshold calculation), centroids updating, and distance computations in the second version. CUDA version 6.0 was used to harness dynamic parallelism in the third version. Two variants of parallel k-means were performed in OpenCL, with distance computation done in parallel at first. In the second version, error evaluation (threshold calculation), centroids updating, and distance computations were all done in parallel. In sequential processing, CUDA versions obtained a speed increase of over 150 times. It enabled real-time processing in surgical procedures while also overcoming computational difficulties.

The different approaches of clustering used for HSI segmentation are shown in Fig. 15.

Chen et al. [21] used an upgraded OPF clustering to accomplish remote sensing picture segmentation, which was inspired by [69]. It was hypothesised that the cluster centres had a high local density, whereas the samples around them had a low local density. As a result, the cluster centres were far apart from samples with higher density values. This segmentation algorithm was applied to five images from the CBERS-2B, Landsat-5, Geoeye, Ikonos-2 MS, and Landsat-8 satellites, all of which covered distinct parts of Brazil. The work was evaluated using the Davies-Bouldin (DB) and Adjusted Rand (AR) indexes. The disadvantage was that it was reliant on the distance function.

Defective potatoes were segmented and classified by [40]. Masking was used to remove the background interference. Moving window fitting polynomial smoothing Savitzky-Golay (SG) filter was used to pre-process spectral data. In their tests, the authors employed K-means clustering segmentation. Combining clustering with SVM enhanced the accuracy of the experiments by 90%. The clustering results are shown in Fig. 16.

On brain MR images, [98] were motivated by the image segmentation results of [20] and [86]. Individual features and structure of multi-modal and imbalanced data were not prioritised in earlier versions of FCM. To achieve robust clustering and represent ambiguous and multi-modal data, intuitionistic Fuzzy C-Means (FCM) clustering with multi-kernel mapping was utilised. To indicate the level of uncertainty of each class in clusters, membership, non-membership, and hesitation degrees were utilised. Individual kernel spaces were mapped to groups of features, and kernels were mixed using optimal weight. The technique achieved high performance and robust clustering on a synthetic HSI data from machine

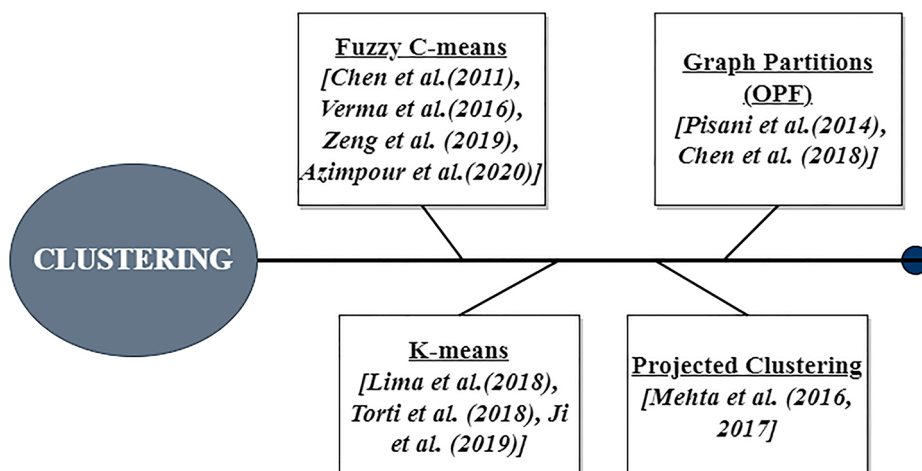


**Fig. 15** Different methods of clustering in survey

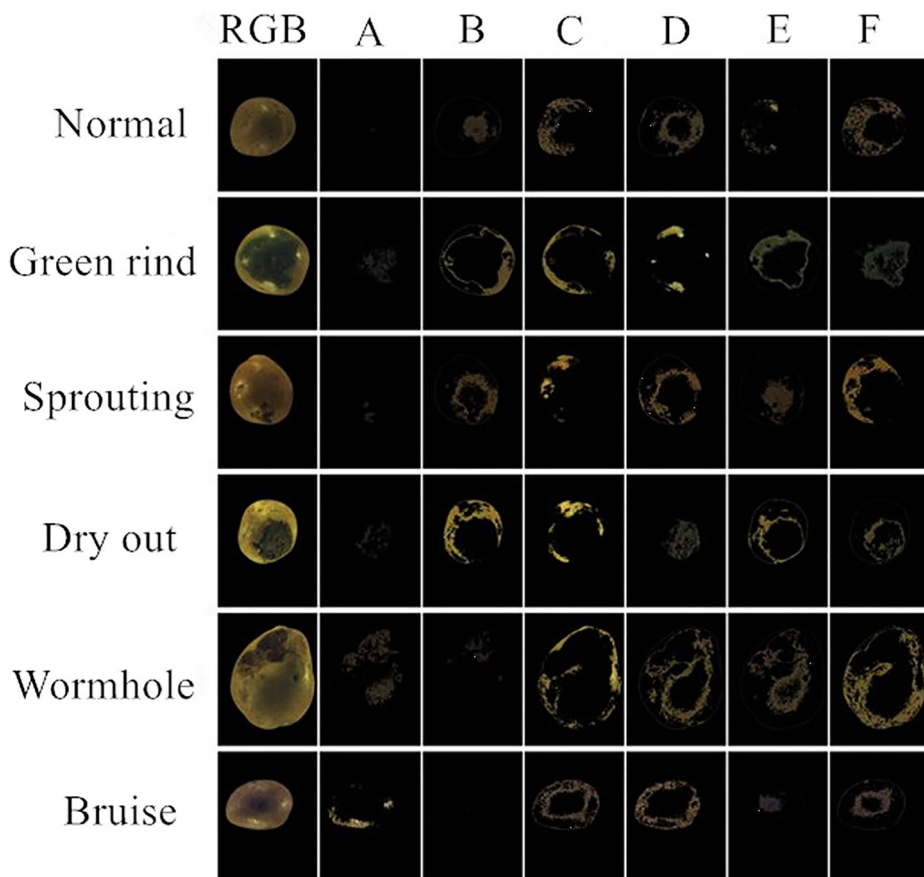


**Fig. 16** Clustering segmentation results, [40]

learning repository. However, having prior knowledge of the data when selecting kernels may aid enhance performance in the future.

Dutta et al. [26] were motivated by quantum based metaheuristics to choose the best number of clusters automatically. A qutrit-based Particle Swarm Optimization (PSO)-based automatic clustering mechanism was proposed. The correlation coefficient was utilised to reduce the dimension, resulting in non-overlapping bands. The information contained in these groups was assessed using Shannon entropy, and the bands with the most information were chosen. To reduce space and temporal complexity, the qutrit states were superpositioned. A random qutrit population was initialised, with all three states being equal. The distance from the active cluster centre was calculated for each pixel, and the pixel was assigned to the cluster with the highest attraction. In terms of PSNR, Dice similarity index, Jaccard index, and computing time, the proposed technique outperformed classical PSO on the Salinas valley dataset.

Albedo recovery based FCM (ARFCM) clustering was applied by [5] to improve the robustness and accuracy of FCM over HSI. To address the complex relationships between neighbouring pixels, albedo and shading elements were used to define pixel values. The different features of elements/objects in HSI were due to their different physical characteristics

which are well described by albedo element. Albedo features extracted more useful thematic spatial information and structures of HSIs. The proposed methodology was applied on Indian Pines, Salinas valley, kennedy space centre and botswana datasets. It obtained high performance in terms of NMI and Adjusted Rand Index (ARI) but it could not determine cluster numbers and had high computation time.

To determine the number of clusters robustly, [12] used Nearest-Neighbour Density Based (NN-DB) methods. It was Based on the principle that cluster centres exhibit higher density than neighbours and are at higher distance from objects having same high density. Clustering was performed using the KNN graph and did not use constant distance parameter. Here, the ‘K’ signified number of NNs which were kept variable. The proposed work had improved ARI and kappa index values as compared to earlier methods of clustering involving fixed-K and constant distance cutoff parameter. The comparative analysis of various Clustering segmentation techniques has been discussed in Table 2.

**Table 2** Comparison analysis of clustering

Authors	Methodology Used	Evaluation Parameters
Chen et al. [20]	Multiple kernel fuzzy c-means	OA of 87% on brain images.
Mehta and Dikshit [59]	Projected clustering, region merging based on spectral similarity and spatial adjacency, CCL, PE.	• Sa : Purity-0.7766 and NMI-0.8102. • PU: Purity-0.7231 and NMI-0.5299.
Mehta and Dikshit [60]	• Projected clustering, MI, k-means, MNN.	• Sa: OA-82.06% • PU: OA-57.98% • DC image: OA-81.58%
Lima et al. [51]	HCA, KMCA for segmentation of FTIR HSI	Better separation of different tissues of skin in HCA.
Torti et al. [83]	OpenMP, OpenCL and CUDA parallel architectures, k-means clustering	CUDA versions achieved very high speed up of almost 150 with respect to sequential processing.
Chen et al. [21]	OPF clustering	• CBERS-2B: DB index-0.5571 and AR index-0.2789. • Landsat-5: DB index-0.5055 and AR index-0.4718. • Ikonos-2 MS: DB index-0.525 and AR index-0.1716. Geoeye: DB index-0.5571 and AR index-0.2591
Ji et al. [40]	Background masking, LDA and SVM during training, k-means clustering during testing.	OA of 90%
Zeng et al. [98]	Intuitionistic FCM clustering, multi-kernel mapping.	Achieved high accuracy and robust clustering in presence of noise as well.
Dutta et al. [26]	Qutrit based PSO, band fusion using ISD, Superior to classical PSO.	• PSNR = 6.48. • JI = 0.5 • DSI = 0.66
Azimpour et al. [5]	ARFCM clustering, albedo features set.	• IP:NMI-0.5059 and ARI-0.2960. • Sa:NMI-0.8127 and ARI-0.6245. • KSC:NMI-0.6752 and ARI-0.4754. • Botswana: NMI-0.6252 and ARI-0.4004.
Cariou et al. [12]	Nearest neighbour Density based method, MNN, KNN	• ARI of Sa - 0.67 and k - 0.76

### 3.3 Watershed segmentation

Angulo et al. [3] used the multi-scale stochastic watershed approach to accomplish unsupervised HSI segmentation. Unlike traditional watershed, it was designed to detect and regularise picture contours that were resistant to altering segmentation settings. Monte Carlo simulations were used to calculate the pdf of the image's contours. There were two multi-scale techniques used. Initially, linear space was employed with Gaussian filters, which gradually simplified the structures and faded the low contrast outlines. In the second technique, non linear morphological scale space was used with levelling to simplify textures and remove minor details. Finally, the contours' pdf was segmented using the non-parametric waterfalls algorithm. Indian Pines and Pavia University were used to test the approach. For better classification, work should be explored by combining the spectral and spatial information of each pixel.

The pixel wise segmentation and classification of HSI often lacked spatial information. Hence, [77] used spectral spatial segmentation and classification methods. Gradient images were formed using four different methods. In first method, one band was manually chosen on which morphological gradient was applied. In second approach, Vectorial gradient with Robust Color Morphological Gradient (RCGM) was applied that removed the farthest pixels. In third approach of multidimensional gradient method, gradients of every band were constructed and combined in weighted summation. Lastly, authors combined watershed segmentation maps of different bands gradients. The results of SVM were refined with watershed regions using majority voting. The RCMG approach gave best results for Pavia University. Sum of gradients of bands performed well for Indian Pines dataset.

Watershed segmentation was used by [46] to detect bruising on peaches. It was used in conjunction with hyperspectral imaging in the Short-Wave Near Infrared (SW-NIR) and Long-Wave Near Infrared (LWNIR) bands. Watershed was applied to multispectral Principal Component (PC) images via morphological gradient augmentation, reconstruction, and marker extraction. Ostu and global threshold performed worse than the proposed technique. The SW-NIR imaging approach properly identified 96.5% of bruised and 97.5 % of sound peaches.

Li et al. [47] used improved watershed segmentation and PCA to detect early deterioration in apples (2019a). As illustrated in Fig. 17, morphological filtering, gradient reconstruction, and marking constraint based watershed segmentation were used. The PCA method was used to extract key wavelengths. PCA was re-implemented on selected wavelengths for processing multispectral images after masking the background to prevent interference. The image with the greatest contrast between decay and sound tissues, on which better watershed segmentation was used, had the highest PC score. It outperformed classic segmentation techniques such as Otsu and global/fixed threshold. PC3 score images accurately detected 99% of decaying fruit and 100% of sound fruit.

A similar approach using PCA with improved watershed and Bi-dimensional Empirical Mode Decomposition (BEMD) was implemented by [48]. With the help of thresholding and binary masking, the fruit was separated from the background interference. To choose informative seven bands, PCA was repeated on the selected PC images. By dividing image signal into several frequency scales, BEMD was used to eliminate noise, enhance, and rebuild images. The noise in the high frequency image was collected, and the scales that followed depicted the texture of oranges. The decay region was segmented using an improved marker controlled watershed method. The results outperformed Otsu thresholding with an accuracy of 97.3% and 100% in detecting sound and decaying zones, respectively.

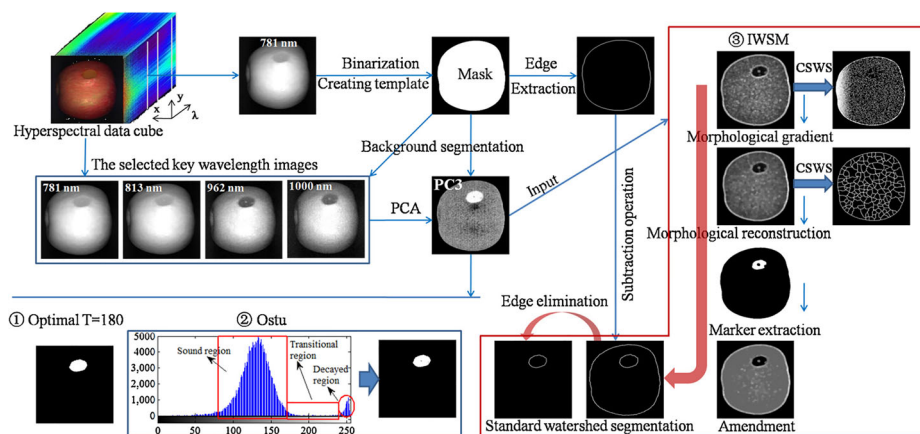


**Fig. 17** Steps of Watershed Segmentation for decay detection in apples [47]

With the use of PCA, pseudo-color transformation, and better watershed segmentation, [80] discovered the deteriorated region on the citrus fruit. Binarization was used to remove the backdrop from the fruit's centre and stem end portions. Using the PC3 image, the decay segmentation was improved. The G component of PC3's pseudo-color was used to improve the contrast between sound and decaying regions. Improved marker controlled watershed technique with morphological gradient enhancement and reconstruction was used to segment the data. The accuracy of the results for detecting decaying and sound fruit was 93% and 96%, respectively.

Chu et al. [23] used Pixel-Wise (PW) and Object-Wise (OW) sampling methodologies to identify diseased maize kernels using Otsu thresholding and watershed. ENVI software was used to manually select ROIs for both PW and OW. PCA and SPA were used to remove redundant data. The authors used the PC1 score image for Ostu thresholding and watershed segmentation after using PCA. Both techniques worked by removing backdrop and separating touched kernels respectively. The accuracy of the OW-PCA-SVM was 99%. The accuracy of OW-SPA-SVM was 100%. In pixel wise analysis, 90.95% and 96.89% accuracy were recorded using PCA-SVM and SPA-SVM, respectively.

The different approaches of watershed used for HSI segmentation are shown in Fig. 18.

Akbari [1] concentrated on enhancing HSI's spectrum spatial classification. Gabor and wavelet transform filters were used to extract the textural features. The Weighted Genetic Algorithm (WGA) was used to reduce reliance between spectral and spatial features. Watershed segmentation map and SVM were utilised to create a marker controlled Minimum Spanning Tree (MST) classification framework. On the Pavia University dataset, the work received an OA of 96.7%.

On multi-colored yarn-dyed fabrics, [42] applied the watershed method. The images were converted to grayscale using Frechet distance, and colour segmentation maps were created using watershed. Using k-means clustering, the over-segmented regions were combined. When compared to traditional k-means, FCM algorithms, these strategies increased execution efficiency by 55%.

Recently, [14] utilised spectral and spatial features to segment HSI in a novel way. Watershed classifier was used instead of softmax classifier in a simple Convnet deep learning

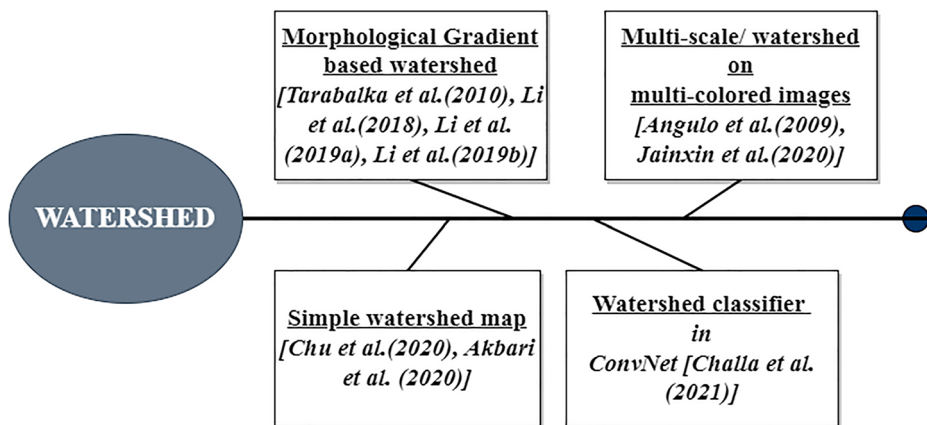


**Fig. 18** Different methods of watershed segmentation in survey

architecture. It achieved maximum margin partition in a similar way to SVM and had comparable performance to Random Forests. To compute loss and derive parameters for neural networks, the authors employed triplet loss. Various state-of-the-art methodologies were outperformed by the work. The comparative analysis of various Watershed segmentation techniques has been discussed in Table 3.

### 3.4 Morphological segmentation

Extended Morphological Profiles (EMPs) were introduced by [7] for structural segmentation of HSI. It entailed performing repetitive PC opening and closing activities. On the Washington DC Mall dataset, a Neural Networks classifier with an OA of 98.9 was used in this work.

Castaings et al. [13] used EMPs on informative bands rather than a single band for morphological operations. Various feature extraction approaches were used to extract and compare distinct EMPs. The following approaches were used: PCA, Gaussian Kernel PCA (KPCA), Nonparametric Weighted Feature Extraction (NWFE), Bhattacharyya Distance Feature Selection (BDFS), and Decision Boundary Feature Extraction (DBFE). On the Pavia University dataset, SVM and RF were utilised for classification. In terms of RF classification, NWFE came out on top, with an OA of 91.2 %. In SVM classification, BDFS fared better, with an OA of 92.3 %.

MPs were created by carrying out procedures with predefined shapes of Structuring Element (SE) that were susceptible to salt and pepper noise. To overcome this limitation [58] employed varied shapes of SE to partition different objects in HSI and enhance classification accuracy. Along with SVM classification, a number of SE forms such as disc, line, diamond, and square were employed. On Pavia University, the paper had an OA of 84.99 %.

Gu and Liu [35] used Sample Screening Multiple Kernel Learning to classify the limited HSI samples (S2MKL). The probability distributions of the training samples were used to adaptively screen them. A linear combination was used to find the appropriate weights of subsets of samples supplied into distinct SVM base kernels. Authors used erosion and dilation procedures to extract MPs instead of the original spectra. MP offered spatial and spectral features that were employed in the Adaboost strategy's multiple kernel learning.

**Table 3** Comparison analysis of Watershed segmentation

Authors	Methodology Used	Evaluation Parameters
Angulo et al. [3]	Multiscale stochastic watershed, Linear space using Guassian filters, Non-linear morphological scale space using leveling, Gradient images, watershed segmentation map.	NA
Tarabalka et al. [77]	Acquired images in sW-NIR and LW-NIR region, PCA, Watershed based on morphological gradient enhancement, reconstruction and marker extraction.	• IP - OA=93.78% and k=92.88%. • PU - OA of 85.42% and k=81.3%.
Li et al. [46]	Morphological filtering, gradient reconstruction and marking constraint based watershed, PCA.	96.5% of the bruised and 97.5% of sound peaches were correctly identified using SW-NIR imaging method.
Li et al. [47]	Combination of improved watershed and BEMD	98% of decayed fruit and 97.5% of sound fruit were identified accurately using PC3 score images.
Tian et al. [80]	Used PCA, pseudo-color transformation and improved watershed segmentation, Background removal using binarization.	accuracy of 97.3% and 100% in detection of sound and decayed regions.
Chu et al. [23]	PW and OW sampling strategies, manual selection of ROI, PCA, SPA, Ostu thresholding and watershed segmentation	An accuracy of 93% and 96% for detection of decayed and sound fruit.
Akbari [1]	Gabor and wavelet transform filters, WGA, watershed map, SVM, marker controlled MST	• The OW-PCA- SVM achieved an accuracy of 99%. • OW-SPA-SVM got an accuracy of 100%. • OW-PCA- SVM gave 90.95% accurate results. • 96.89% accuracy of OW-SPA-SVM.
Jianxin et al. [42]	Frechet distance, watershed map, k-means clustering	PU - OA = 96.7% and k=0.948.
Jianxin et al. [14]	Watershed classifier in Convnet deep learning architecture	NA • For IP - OA=99.98% and k=0.999. • For KSC - OA = 99.72% and k=0.996.

This strategy, which was tested in the Indian Pines, Salinas Valley, and Pavia University, outperformed other state-of-the-art approaches.

The geometrical characteristics were not properly exploited by MPs based on preset SE values. Kumar and Dikshit [45] used EMPs to extract useful structural information by using many SE shapes instead of just one. Multiple classifiers were utilised in two supervised classification frameworks. The EMPs were classified separately, and a final classification map was created via decision fusion. The first approach used PCA to reduce dimension and a probabilistic classifier to classify each EMP. Two-tier decision fusion was used in the second framework. On the Pavia Centre, Pavia University, and Salinas Valley datasets, SVM and RF classification were used. On the same, OAs of 99.82%, 98.30%, and 98.57% were achieved, respectively. The technique was noise-resistant and delivered accurate classification results.

The different approaches of morphology used for HSI segmentation are shown in Fig. 19.

Hu et al. [38] performed two steps of spectral-spatial HSI classification. Morphology was used to post-process the results of the guaussian kernel SVM classification (MM). To reduce noise, the SVM multi-class results were converted into multiple binary classification results using MM. A pixel corresponding to the investigated class was given a value of 1 and a value of 0 otherwise. When compared to other state-of-the-art post-processing techniques, the method attained an accuracy of 93.74% on the Indian Pines dataset.

Song et al. [73] focused on positive lung cancer identification in HSI. Segmentation mechanism consisted of SVM, majority analysis and clumping processing. After SVM, the misclassified pixels were removed using majority analysis. In the end, Clumping process used morphological closed operation to remove gaps and combine adjacent similar pixels. It achieved an accuracy of 90.6% and 91.1% for detection of lung cancer negative and positive cells, respectively. The segmentation results have been shown in Fig. 20.

Beirami and Mokhtarzade [6] used SuperPCA to group bands and extract characteristics. PCA was used to extract useful bands from superpixels. SuperPCA was superior to PCA because it included more contextual data. EMPs were employed to improve segmentation results. Maximum Likelihood and NN classifiers were successfully implemented. On Pavia

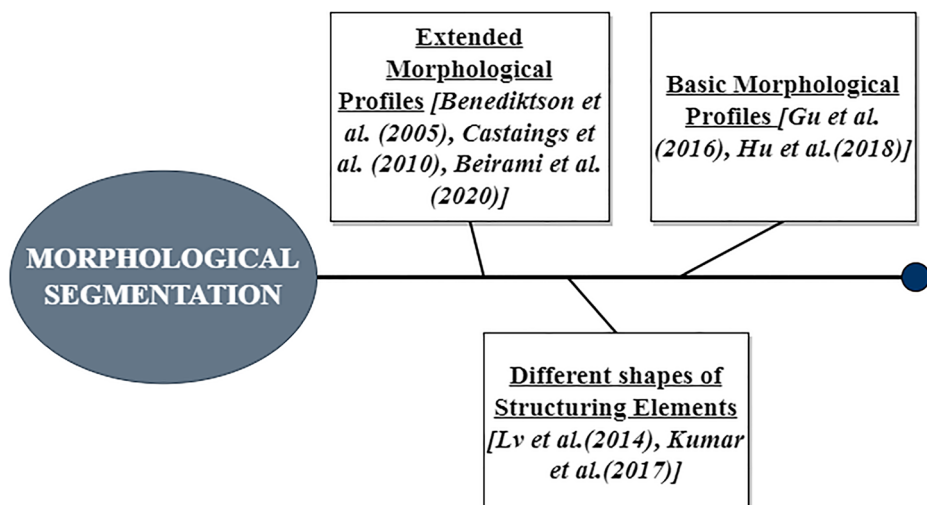


**Fig. 19** Different methods of morphological segmentation in survey

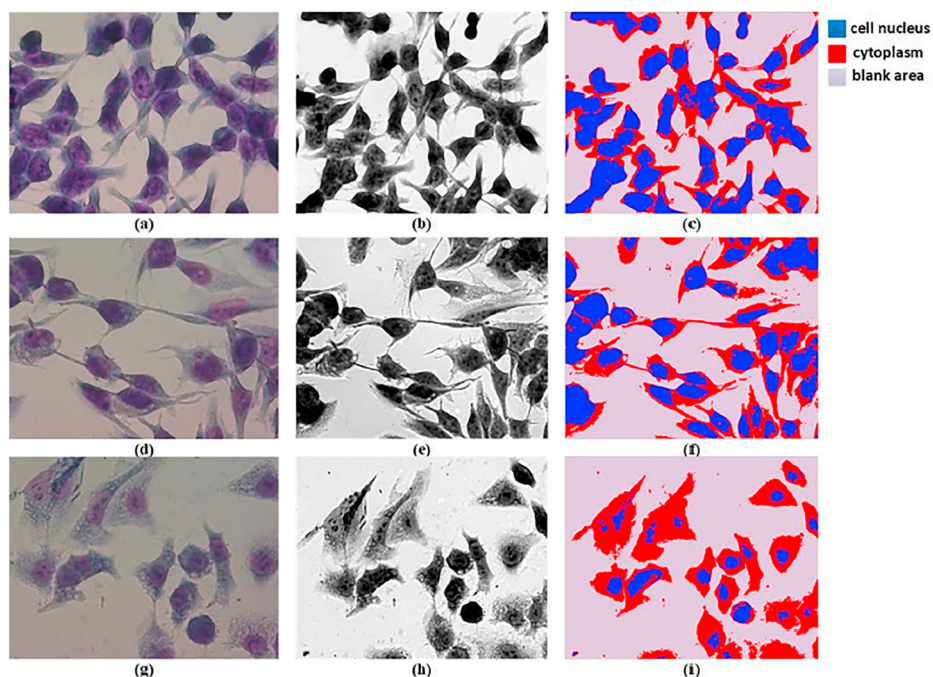


**Fig. 20** Morphological segmentation results [73]

University, their work received an OA of 94.91%, and on Salinas Valley, it received an OA of 99.54%.

Morphological approaches were used on HSI sceneries with objects of various shapes and sizes. Lu and Hu [57] observed that extracting spatial properties of essential objects becomes more challenging as a result of this. As a result, a two-stage structure was created to handle the same issues. Saliency Profiles (SPs) were created in the first stage utilising grayscale contrast and edge information. It aided in the extraction of objects with significant local maxima in their saliency index. Morphological traits were used to build hierarchical spatial features. Adaptive superpixels were created in the second stage employing SPs. To create a classification map, the collected superpixel features were combined with spectral data. On Indian Pines, 99.41% on Pavia University, and 98.74% on Pavia Centre, this strategy obtained an OA of 97.72%. The comparative analysis of various Morphological segmentation techniques has been discussed in Table 4.

### 3.5 Edge detection based method

By incorporating edge information, [78] used Markov Random Field (MRF) regularisation to refine the classification map of SVM. The Maximum A-posteriori-MRF (MAPMRF) framework assumed that a pixel belonging to one class would have pixels belonging to the same class as its neighbours. It also concentrated on lowering the image's overall energy. To keep the edge, the authors included a Fuzzy edge/no-edge function in the MRF's spatial energy function. The average of four directional gradients generated using the Sobel mask was used to construct one band gradient. In the fuzzy function, this one-band gradient was

**Table 4** Comparison analysis of morphological segmentation

Authors	Methodology used	Evaluation parameters
Benediktsson et al. [7]	EMP, repetitive opening and closing operation, Neural Network classification	Highest OA of 89.4% on PU
Castaings et al. [13]	EMPs, NWFE, BDFS feature extraction methods, SVM classification	<ul style="list-style-type: none"> <li>In case of RF classification, NWFE performed the best and gave an OA of 91.2%.</li> <li>BDFS performed better in SVM classification and achieved an OA of 92.3%.</li> </ul>
Lv et al. [58]	Different shapes of Structuring Elements, SVM.	OA of 84.99% on Pavia University.
Gu and Liu [35]	Morphological profiles provided with spatial and spectral features, sample screening multiple kernel learning, SVM classification.	<ul style="list-style-type: none"> <li>IP: OA-93.30% and AA-95.52%.</li> <li>PU: OA-96.03% and AA-96.36%.</li> <li>Sa = : OA-94.78% and AA-97.15%</li> </ul>
Kumar and Dikshit [45]	EMPs, Different SEs having different shapes.	<ul style="list-style-type: none"> <li>PU - OA=98.30% and k=0.978.</li> <li>Sa - OA-98.57% and k=0.984.</li> </ul>
Hu et al. [38]	Mathematical morphology for post processing and noise removal, Gaussian kernel based SVM classification	For IP - OA = 93.74% and k=0.926
Song et al. [73]	Morphological closed operation, SVM classification	Accuracy of 90.6% and 91.1% for detection of lung cancer negative and positive cells, respectively.
Beirami and Mokhtarzade [6]	EMPs, SuperPCA, Maximum Likelihood, NN classification	<ul style="list-style-type: none"> <li>PU - OA = 94.91% .</li> <li>Sa - OA = 99.54% .</li> </ul>
Lu and Hu [57]	Saliency Profiles (SPs), morphological operations for spatial features, adaptive superpixels.	<ul style="list-style-type: none"> <li>IP - OA = 97.72%.</li> <li>PU - OA = 99.41% .</li> </ul>

used. The experiment using the Indian Pines, Pavia University, and Pavia Centre datasets yielded OAs of 92.05%, 87.63%, and 97.60%, respectively.

Spectral spatial segmentation classification was also used by [30]. MRFs would result in over smoothing, hence the Sobel edge detection method was utilised to maintain the edges. On Indian Pines, the accuracy was 90.50%, and on Salinas Valley, it was 97.24%.

Youn and Lee [95] segmented images using Bhattacharya distance which determines how similar two neighbouring blocks are. Each pixel's neighbourhood blocks were considered to acquire edge information. Horizontal, vertical, and diagonal edges emerged as a result of this. Weiner filtering was used to remove noise, while PCA was used to minimise the dimensions. The maximum Bhattacharya distance was used to find the final edge information. It discovered edges that were difficult to trace better than the Sobel approach.

Xia et al. [92] used ensemble strategy where Independent Component Analysis (ICA) selected spectrally independent components followed by Edge-Preserving Filtering (EPF). Rolling Guidance Filter (RGF) was applied which removed small structures.

Cui et al. [24] proposed segmentation and edge preserving filtering aided spectral-spatial classification. Visible, infrared and short wave infrared bands were partitioned into smaller subsets of K number of adjacent bands. To reduce noise and dimension averaging method was applied to merge subsets of adjacent bands. Recursive EPFs namely, joint bilateral and domain transform were applied to obtain one feature band. With the e-Cognition software,

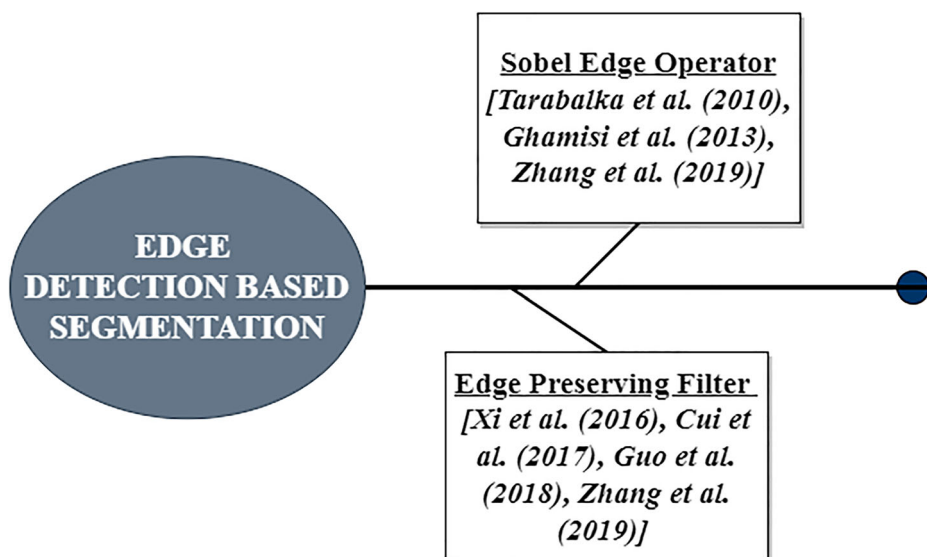


**Fig. 21** Existing edge based segmentation techniques

spatial features were extracted based on color and shape criterion. The SVM classification results were refined using joint bilateral filtering. It outperformed existing methods like SVM and simple EPF.

The different approaches of edge detection used for HSI segmentation are shown in Fig. 21.

Guo et al. [36] performed segmentation using a combination of Joint Representation KNN (JKNN) algorithm with Front Guided Filter (FGF). PCA provided the guidance images for the guided filter. In one method named FGF-JKNN, JKNN was combined directly with the FGF. FGF extracted spatial features which were fed to KNN. In the second method, JKNN was used with posterior guided filter. The guided filter optimized the classification map produced by JKNN and converted it into probability maps. It chose the maximum probability of every pixel as the final classification result. The methodology was implemented using Indian Pines and Pavia University dataset where PGF-JKNN improved the OA, AA and kappa coefficient by 4% as compared to several state-of-the-art classification approaches.

Zhang et al. [100] extracted features of HSI using EPFs. The spectral dimension was reduced using averaging method. Structure edge detectors on first three PCs gave edge probability map. The reduced dimensions and learned edge maps were combined with Domain Transform Recursive Filtering. Indian Pines and Salinas valley dataset were classified using SVM. The technique achieved an OA of 80.17% and 97.92%, respectively.

In an ensemble learning architecture, [87] used multi scale EPFs and the SUSAN edge detector. At various degrees of smoothing, multi-scale BEEPS extracted spectral-spatial characteristics. Single scale BEEPS features were employed as inputs to Stacked Sparse Autoencoders and Random Forest (SSARF). The ensemble's probability outputs were merged using the majority voting process. To increase accuracy, the SUSAN edge detector combined the classification findings with the unlabeled samples' neighbouring spatial information. The Indian Pines and Pavia University datasets were used to test the approach.

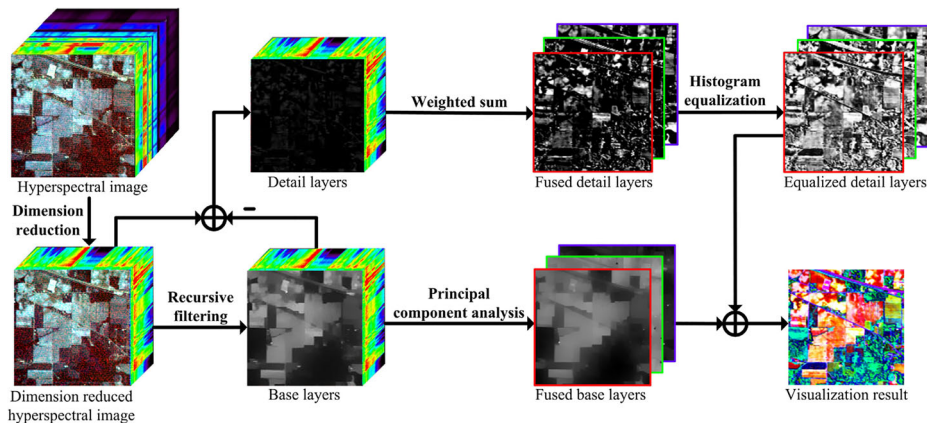


**Fig. 22** Steps of edge preserving filtering based technique [44]

The BEEPS parameters, such as degree of blur and smoothness, were carefully selected to determine the performance.

PCA and DTRF were used by [44] to visualise the hyperspectral images. Edge preserving DTRF extracted base and detail layers. The weighted sum approach was used to combine the Base layers with PCA and the Detail layers. The fusion weights were derived using a transform matrix of base layers in the latter. Histogram equalisation was employed to enhance the contrast of fused detail layers before they were combined with the fused base layer. Four hyperspectral datasets, including Indian Pines, Pavia University, Urban Data, and Washington, were processed using the manner shown in Fig. 22. Separability of Features (SF), Standard Deviation (SD), Average Gradient (AG), and Entropy (E) were among the quality measures employed. The degree of colour space mapping between various pixels was indicated by SF. The produced image's contrast level was measured using SD. E is the amount of information in the final image, while AG indicated the clarity of the image. The effort resulted in increases in SF, SD, AG, and E by 80.45%, 69.29%, 138.61%, and 23.21%, respectively. The technique made advantage of two image scale properties. By using the hit and trial method, the filter's settings were set. The multi-objective evolutionary optimization algorithm may be used to help set the parameters in the future.

Zhang et al. [99] identified frost damaged rice seeds in hyperspectral imaging covering spectral range 866.4 nm - 1701.1 nm. Binarization was done to form mask that extracted the seeds as ROI and removed background interference. The authors employed the sobel edge detection operator and morphological processes to derive the average spectral reflectance of each pixel of ROI at each wavelength. PCA, Neighborhood Component Analysis (NCA), and SPA were used to extract the ideal wavelengths. Implemented models included Deep Forest (DF), DT, KNN, and SVM, which produced acceptable results. The comparative analysis of various Edge Detection based segmentation techniques has been discussed in Table 5.

### 3.6 Superpixel segmentation

Stacked Denoising AutoEncoder (SDAE) was utilised by [54] to learn spectral features representation of the data and project the features into PCA space. Superpixels were used to combine spatial data for the sake of improving the outcomes of the spectral categorization.

**Table 5** Comparison analysis of Edge detection based segmentation

Authors	Methodology used	Evaluation parameters
Tarabalka et al. [78]	Probabilistic SVM, MRF regularization, Fuzzy edge/no-edge function, integrated in spatial energy function of MRF.	• IP: OA-92.05%. • PU: OA-87.63%.
Ghamisi et al. [30]	Hidden MRF, SVM classification, edge smoothing using Sobel edge detection	• IP: OA of 90.50%. • Sa : OA of 97.24% .
Youn and Lee [95]	Bhattacharya distance, PCA, Weiner filtering. In comparison with sobel edge detection and segmentation method, proposed work detected edges which were difficult to trace.	NA
Xia et al. [92]	EPF, ICA, RGF	NA
Cui et al.[24]	Joint bilateral and domain transform filters, eCognition software based on color and shape criterion, SVM classification.	• IP: OA-95.5%, AA-94.67% and k-94.91. • PU: OA-95.51%, AA-93.90% and k-94.08. • Sa: OA-98.67%, AA-98.96% and k-98.52.
Guo et al. [36]	Joint representation KNN algorithm with front and posterior guided filter, PCA.	• IP: OA-97.26%, AA-95.90% and k-96.88. • PU: OA-98.18%, AA-97.60% and k-97.58
Zhang et al. [100]	DTRF, SVM.	• IP: OA-80.17%. • Sa: OA-97.92%
Wan and Zhao [87]	Ensemble learning based architecture, multi scale edge preserving filtering, SUSAN edge detector, Stacked sparse autoencoders and RF.	• IP: OA-94.04%, AA-90.82% and k-93.20. • PU: OA-99.53%, AA-99.43% and k-99.37.
Kang et al. [44]	Averaging based image fusion, Domain transform recursive filter, PA.	Increased the quantitative metrics Separability of features, Standard Deviation, Average Gradient and Entropy by 80.45%, 69.29%, 138.61% and 23.21%, respectively.
Zhang et al. [99]	Sobel edge detection operator, morphological operations- corrosion and dilation, DF, Decision Tree, KNN, SVM.	NA

Higher spatial, spectral, and feature consistency pixels were assumed to belong to the same label. The experiment was conducted on Indian Pines, Pavia Center, Pavia University, and Salinas Valley using various resolutions of superpixel, and the maximum overall accuracy was 91.9%, 99.8 %, 96.4%, and 95.5 %, respectively.

Yu et al. [96] developed a multiscale superpixel segmentation and using a subspace-based SVM (SVMsub) to get classification maps while reducing dimensionality. The spatial segmentation maps and HSI spectral characteristics were combined in the subspace projection. The pixel level data was represented as superpixel-level data, and it was done using a feature fusion technique at various sizes. In comparison to other spectral spatial approaches like SVM, SVM-Markov random fields (MRF), and SVMsub MRF, the methodology used on the Indian Pines and Pavia University datasets produced higher results and accuracy.

Weighted Spatial Correlation Representation was utilised by [84]. (WSCR). It calculated the spectral correlation coefficient among pixels in the superpixel zones that were clustered locally. Due to the high information of spatial and structural features, the first three PCs were selected as base images for superpixels segmentation. The Entropy Rate Segmentation (ERS) algorithm was used by the authors to create superpixels. The datasets Indian Pines and Washington, DC were used, where the maximum accuracy of 95.36% and 97.9% was obtained, were used.

Cao et al. [10] classified non-overlapping hyperspectral images using superpixels produced by ERS. To provide non-overlapping training and testing sets, a controlled sampling approach was used. The training samples were handled as Regularized Affine Hulls and seen as a single set with similar labels (RAHs). Every two Regularized Nearest Points (RNP) were chosen using an iterative process. Labels were given to the testing set based on the proximity of the training sample and the distance between the two RNP. On the Indian Pines, Salinas valley, and Botswana data sets, the experiment obtained the maximum OA of 82.79%, 87.07 %, and 95.18 %, respectively.

The different approaches of superpixel generation used for HSI segmentation are shown in Fig. 23.

Zhang et al. [101] performed semi supervised based Simple Linear Iterative Clustering segmentation for HSI. The superpixel map and initial classification map was used to select pseudo-labeled samples (PLSs). The PLS were labels given to unknown samples of same superpixel using known labeled samples. The final classification map of SVM was obtained by integration of labeled training samples and PLSs. The proposed work obtained OA of 95.01% on Indian Pines, 97.51% on Pavia Data and 99.21% on Salinas valley.

Wang et al. [88] used multiscale superpixel segmentation to get around the problems of utilising a single kernel for multi-feature data and failing to capture comprehensive information. Using ERS, which preserved image edge information, the first PC image was utilised to create superpixel at various scales. Multiscale weighted spectral-spatial kernel and the original spectral-spatial kernel in SVM were used to create a synthetic kernel. The classification accuracy of 98.53% was obtained on Washington DC's mall dataset.

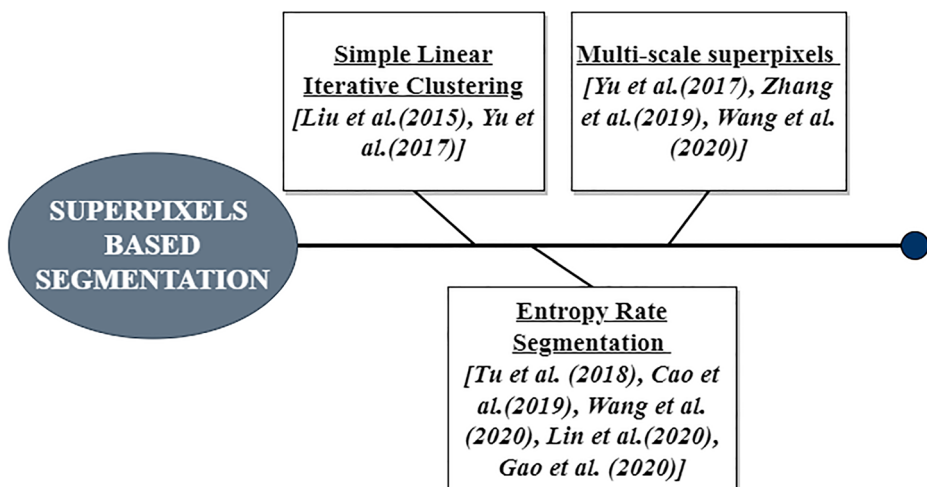


**Fig. 23** Different methods of Superpixel segmentation in survey

Lin and Zhang [52] proposed superpixel segmentation of HSI using MI and entropy. Shannon entropy initially calculated the information of the image and selected certain spectral bands above a chosen threshold. MI further removed redundant bands. MI and Color Matching Functions (CMF) together used color uniformity and edge smoothness functions to select most useful bands. These bands created a false color image. Hence, superpixel segmentation of the false color images was based on entropy, MI with Color Histogram Driving (IM-CHD) and hill climbing optimization. Indian pines and Pavia Centre dataset were used on which these techniques performed better than other state of the art methods.

A composite Spectral-Spatial Kernel for Anomaly Detection (SSKAD) was employed by [28]. This kernel included spectral information as well as spatial information from superpixels. In contrast to prior detection models that operated in linear space and only used spectral information, it took into account non-linear aspects of the data. The Reed-Xiaoli anomaly detection algorithm was used to build the detection map. It created decision rules to differentiate between text pixels and backdrop using Mahalanobis distance. The work was carried out using actual datasets collected by the HYDICE, ROSIS, and AVIRIS sensors over Pavia and the San Diego area, respectively. When compared to state-of-the-art anomaly detection approaches, it performed better in terms of Receiver Operating Characteristic (ROC) curve and Area Under the ROC curve (AUC).

A multiple kernel technique involving spectral, spatial and semantic information using SVM was implemented by [89]. Through first 3 PCs, Gabor features, ERS superpixel segmentation map and EMPs were acquired. For uniformity in spatial characteristics, mean filtering within each superpixel was done. To gain semantic information, k-means clustering map and segmentation map on each superpixel was performed. Authors treated each superpixel as a separate document/image. Spectral features, ERS map and manually decided ‘k’ number of cluster centroids created semantic features using Bag of Visual Words (BOVW). To create visual dictionary, K-means clustering was performed on the spectral features and clustered them into ‘k’ cluster centres. Creation of  $k \times 1$  histogram feature vector was done for each superpixel. For final results, composite kernel with SVM was applied using weighted sum of above stated kernels. The work was implemented on Indian Pines and Pavia university and obtained highest overall accuracy of 98.39% and 99.77%, respectively.

Cao et al. [11] improved HSI prediction using both spectral and spatial features. To obtain enhanced spectral features, cascaded SVM were used where information predicted by precedent layer gave better predictions in the subsequent layers. To obtain spatial information at different scales superpixel segmentation was performed. The final label was obtained using majority voting at different scales. It obtained highest OA of 97.68% on Indian Pines, 99.38% on Pavia University and 99.23% on Salinas valley.

To overcome high computation cost of generating superpixels, [71] applied GPU accelerated waterpixel algorithm for superpixel segmentation. In waterpixel, segmentation regions were obtained using 4 stages. Initially, vectorial gradient extracted spectral information. Spatial regularization, marker selection and application of watershed transform was carried on. The methodology obtained high speedup values as compared with multicore OpenMP using 8 threads. The comparative analysis of various Superpixel based segmentation techniques has been discussed in Table 6.

### 3.7 Region based segmentation

Tarabalka and Tilton [79] used hierarchical optimization with probabilistic classification for shape analysis region segmentation. Every iteration of the Probabilistic SVM involved merging the regions with the lowest Dissimilarity Criteria (DC) and recalculating the

**Table 6** Comparison analysis of Superpixel based segmentation

Authors	Methodology used	Evaluation parameters
Liu et al. [54]	Deep network based on SDAE, PCA, Linear Regression Model, Superpixels using SLIC.	• IP : OA-91.9%. • PU : OA-96.4%. • Sa : OA-95.5%.
Yu et al. [96]	Multiscale superpixel segmentation, SLIC, SVMsub, decision fusion, majority voting.	• IP: OA-95.28% and k-0.95. • PU: OA-97.57% and k-0.97.
Yu et al. [84]	Superpixels using ERS, PCA, decision function using WSCR and JSR.	• IP: OA-95.36% and AA-94.59%. • Washington DC: OA-97% and AA-96.27%.
Cao et al. [10]	Controlled sampling strategy, Superpixels using ERS, RAHs and RNPs.	• IP: OA-82.79% and AA-84.56%. • Sa: OA-87.07% and AA-91.73%. • Botswana: OA-95.18% and AA-96.17%.
Wang et al. [88]	Multiscale superpixel segmentation using ERS, PCA, SVM.	Washington DC's mall: OA-98.53%.
Lin and Zhang [52]	Superpixel segmentation using MI with color histogram driving, hill climbing optimization.	Improved ASA, UE and BR results.
Gao et al. [28]	Superpixels using ERS, composite spectral spatial kernel, CKA based cosine similarity, Reed-Xiaoli anomaly detection algorithm	Better performances in terms of ROC and area under the ROC curve.
Wang et al. [89]	Composite kernel based on spectral, spatial and semantic information, Gabor features, ERS based superpixels, EMP features, k-means clustering, SVM classification.	• IP: OA-98.39% and AA-98.30%. • PU: OA-99.77% and AA-99.80%.
Cao et al. [11]	Cascaded SVM, Superpixels at different scales, majority voting	• IP: OA of 97.68% and k=0.975. • Sa: OA of 99.23% and k=0.991.
Quesada- Barriuso et al. [71]	Superpixels using GPU based waterpixel algorithm, CUDA.	–

classification probabilities. After computing the DC between all adjacent regions, the smallest DC was determined, and the regions were merged as a result. The experiment's OA, AA, and kappa coefficient values were 97.12%, 97.03%, and 96.35%, respectively, using the Centre of Pavia dataset.

Using region-growing segmentation, [8] segmented and categorised HSI. The unlabeled samples were tagged using classes from the same region under the assumption that pixels within the same segmented area are homogeneous. On the SVM classification map, an edge-preserving filter was applied to reduce noise and sharpen the edges. Different percentages of the labelled samples from the Indian Pines dataset were used to test the suggested approach. Using less labelled samples, it outperformed SVM, PCA, and Edge Preserving Filter (EPF) approaches in terms of overall accuracy.

Qiao et al. [70] identified and classified fungi contaminated peanuts. Morphological corrosion removed the influence of mixed kernel edges. ANOVA and Non-parametric Weighted Feature Extraction (NWFE) performed features selection and extraction, respectively. Top bands having high F-values were selected and classified pixels using SVM. Region growing

segmented the images as kernel-sale patches. Using the combined result of classification map and region growing segmentation, ratio of number of moldy kernels by healthy kernels was formed to form final identification map. It obtained an accuracy of 96.32%, 94.2% and 97.51% in peanut breed A, B and C, respectively during validation.

Segmentation using classical segmentation techniques was implemented by [63]. Basic Segmentation techniques like watershed, clustering and region growing were employed. To overcome over-segmentation, authors improved the segmented results by region merging using priority queues. It maintained list of adjacent and similar regions. The quality of segmentation was evaluated using Global Consistency Error (GCE) and Rand Index (RI) on Indian pines and Salinas Valley images. K-means clustering obtained best values of GCE while region growing performed better in terms of RI.

The different approaches of region based methods used for HSI segmentation are shown in Fig. 24.

Appice and Malerba [4] created SoCRATE (Spectral-spatial correlation segmentation-based classifier). Spatial dependency of each spectral component was measured with the help of a local indicator. This gave a vector of spatial-spectral features. Authors used region growing contiguity based segmentation which separated the sensed scenes into objects. From these objects, centers of regions were identified. The methodology was carried on Indian Pines, Pavia University and Salinas images where various configurations of SoCRATE were compared using 1-5% training samples of the ground truth data. For the classification of minority classes, an improvement in outlier removal method is needed. Parallel computation architecture could help in real time application. In future, the segmentation could be integrated into iterative active learning for label acquisition.

Region-based heirarchical segmentation based on Binary Partition Trees(BPT) was employed by Ismail and [39]. Through spectral angle mapping, the zones were further combined based on spectral similarity. With the use of PCA, the features were extracted, and a compact BPT was created. The resultant BPT structure was subjected to K-means clustering. On Salinas Valley, an OA of 89.37% was noted.

Akbari [2] used marker based heirarchical region growing segmentation with SVM. With Minimum Noise Fraction (MNF) algorithm, redundant features were removed. For spatial

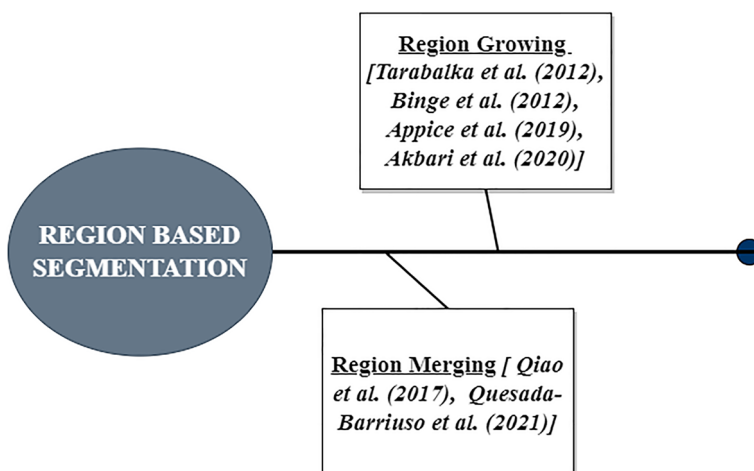


**Fig. 24** Existing region based Segmentation techniques

**Table 7** Comparison analysis of region based segmentation

Authors	Methodology used	Evaluation parameters
Tarabalka and Tilton [79]	Probabilistic SVM, shape analysis segmentation, region merging using DC.	• PU: OA of 97.12%, AA of 97.03% and k = 0.963.
Binge et al. [8]	Segmented and classified HSI in a semi-supervised manner using PCA, region growing, SVM	IP: OA-94.27% and AA-94.48%.
Qiao et al. [70]	Morphological corrosion, ANOVA, NWFE feature extraction methods, region growing, SVM classification	• An accuracy of 96.32%, 94.2% and 97.51% in breed A, B and C of peanut kernels.
Myasnikov [63]	Watershed, clustering and region growing, PCA. Improved segmented results using region merging with priority queues.	• The quality of segmentation was evaluated using GCE and RI. • k-means clustering obtained best values of GCE. • Region growing performed better in terms of RI.
Appice and Malerba [4]	Spectral-spatial correlation, Region growing contiguity based segmentation, SVM classification	• IP : OA- 98.18%, AA-97.93% and k-0.97. • PU : OA-99.84%, AA-99.71% and k-0.99. • Sa : OA- 99.94%, AA-99.93% and k-0.99.
Ismail and Orlandic [39]	watershed, BPT based heirarchical region segmentation, spectral angle mapping, PCA, k-means clustering	Sa : OA = 89.37%.
Akbari [2]	marker based region growing, SVM, MLP classification.	PU : OA of 94.3%.

features, Gabor filter, mean, entropy and contrast were extracted. Both the spectral and spatial features on SVM and Multi Layer Perceptron (MLP) neural network were implemented. The comparative analysis of various Region segmentation techniques has been discussed in Table 7.

### 3.8 Deep learning based segmentation

Lin et al. [53] extracted spatial features using AutoEncoder (AE) and PCA used for spectral dimension reduction. SVM classification was carried out with a single layer of AE. For deep representation, stacked AE with logistic regression technique was performed. The experiment recorded low error rates on Kennedy Space Centre(KSC) and Pavia University.

In order to learn multistage filter banks, binary hashing, and blockwise histograms for indexing and pooling, [15] cascaded PCA. This network was known as PCANet. On benchmark visual datasets for digit and face recognition, the authors implemented PCANet. PCANet served as a useful benchmark against which more sophisticated architectures or processing components could be justified.

With Segmented Stacked AE (S-SAE), [97] performed spectral segmentation of the pixels. It confronted the original features into smaller segments of data which were processed separately by smaller and local SAEs. The complexity was highly reduced with the proposed method. It achieved better accuracy in segmentation and classification of the scenes in Indian Pines and Centre of Pavia dataset. This work could be extended using saliency detection methods, adaptive sparse representation and weakly supervised learning. The major drawback was not extracting the spatial features.

Deep convolutional neural network was used to segment images and enhance their spatial features by [50]. Each band was normalized in the range [0,1]. The authors chose first PC image as reference image due to high spatial information. Gray Level Co-Occurrence (GLCM) was used to extract spatial features like entropy, contrast, correlation, dissimilarity. The authors compared the GLCM features of bands with the specific features of the first PC and used them in a ratio. The band with the lowest ratio value was chosen as the training label. The data was trained using a CNN model with optimum parameters. For additional classification, ELM was used. For smaller training samples from the Indian Pines, Salinas Valley, and Center of Pavia datasets, this combined approach performed well. It performed faster than other state of the art classifiers.

Pan et al. [66] used PCANet [15] as the foundation, where multi-grain and semi-supervised information was integrated. A simplified multi-grained network called MugNet, in which each grain represented a deep learning model, was constructed using three different methodologies. Spectral MugNet and spatial MugNet were two parallel branches of the MugNet. The spectral associations between the bands and the spatial correlation within the nearby pixels were used to create combined spectral-spatial characteristics. Convolutional kernels were created using a semi-supervised method in the second strategy. Last but not least, it lacked any tuning hyperparameters. In compared to other state-of-the-art techniques, it achieved the highest overall accuracy of 90.65%, 90.82%, and 93.15% on the Indian Pines, Grss\_dfc\_2013 and Grss\_dfc\_2014 datasets, respectively. It is necessary to increase computational effectiveness. In the future, MugNet might be changed to operate entirely end-to-end.

Paoletti et al. [67] built a 3D CNN architecture to obtain spectral and spatial features of HSI. The authors processed the border areas of image using border mirroring strategy. The 3D patches were grouped into batches and sent to convolution layers. Four fully connected layers were used and cross entropy was the loss function of CNN. The experiment was performed on Indian Pines and Pavia University dataset. On comparison with 1D, 2D, 3D CNNs and Multi-Layered perceptron, it achieved highest accuracy. The classification accuracy was dependent on manual selection of parameters.

Chen et al. [18] performed joint spatial and spectral features driven HSI segmentation. Image blocks containing local neighbourhood features gave spatial and spectral features. The network was combined with the SVM (RBF kernel) in some of the fully connected layers. For obtaining the features, the first convolution layer was used that was Multi-scale features extraction layer. This layer extracted features invariant of deformation and scaling. The second convolution layer named as feature fusion layer merged the spatial and spectral features. It was followed by features reduction convolution layer. The network obtained an OA of 98.02% on Indian Pines dataset. On combination with SVM, highest accuracy of 98.39% and 98.44% was obtained on the Indian Pines and Pavia University dataset, respectively.

Cheng et al. [22] addressed the issues of poor generalisation of CNN models on small samples. Both spatial and semantic features were exploited using multiple convolutional layers. GoogLeNet, VGG-CNN-S and AlexNet extracted deep spatial features. To further improve accuracy, a unified metric learning framework learnt spectral-spatial features and trained SVM. To achieve this a new objective function was employed which embedded metric learning regularization term into SVM training. Their work achieved better accuracy than other state of the art methods.

Zhou et al. [103] used spectral-spatial Long Short Term Memory (LSTM) networks for segmentation and classification of HSI (Fig. 25). The spectral values of each pixel in all the channels were fed into the Spectral LSTM (SeLSTM). For spatial LSTM, 1st PC

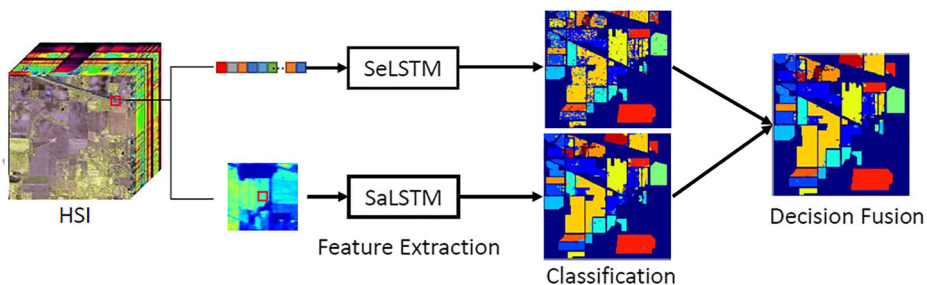


**Fig. 25** Joint spectral spatial based LSTM [103]

image, local patches centered at a pixel and the row vectors of each image patch were used. Figures 26 and 27 display structure of SeLSTM and SaLSTM, respectively. For classification, spectral and spatial features were obtained separately for each pixel. For joint spectral-spatial classification, results of individual LSTMs were intuitively fused in weighted summation. The performance of SeLSTM, SaLSTM and SSLSTMs were compared with several methods. This technique improved the accuracy by at least 2.69%, 1.53% and 1.08% on Indian Pines, Pavia University and Kennedy Space Centre dataset, respectively.

Zhou et al. [104] aimed to reduce within class disparity and increase between class distance. For this, Compact and Discriminative Stacked Autoencoders (CDSAE) were used. CDSAE learned features using Fisher discriminant regularization and to reduce number of neurons, diversity regularization was embedded. This techniques achieved an OA and k of 97.59% and 0.968 on Pavia University, 95.81% and 0.953 on Indian Pines and 96.07% and 0.967 on Salinas Valley, respectively.

Cao and Guo [9] proposed a new architecture for CNN termed as 3D-2D SSHDR. It was an end to end hybrid dilated residual networks. 3D hyperspectral cubes were the input. 3D-2D SSHDR contained five parts, i.e., spectral feature learning process, 3D to 2D deformable part, spatial feature learning process, an average pooling layer, and a fully connected layer. The 3D spectral residual blocks learned discriminant spectral features. For spatial feature learning, the authors converted the extracted spectral features of 3D images into 2D features map. To continue learning discriminative spatial features, hybrid dilated convolution (HDC) residual blocks were used. This helped in increasing the receptive field of the convolution kernel. The network was trained using supervised learning. The experiment achieved an

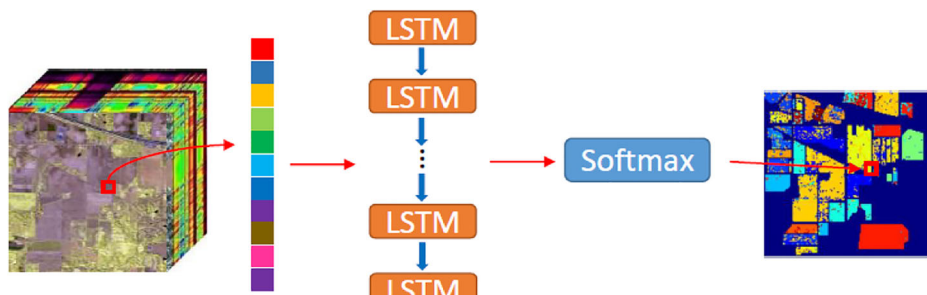


**Fig. 26** Spectral LSTM architecture [103]

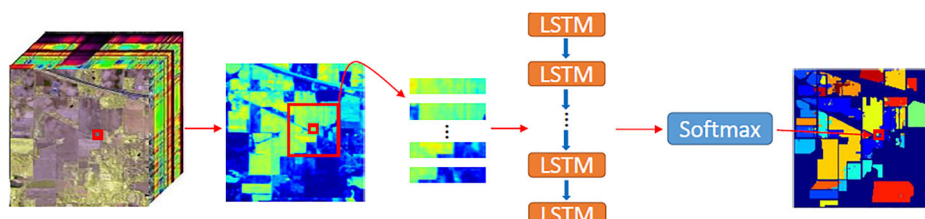


**Fig. 27** Spatial LSTM architecture [103]

OA of 99.46%, 99.89% and 99.81% on Indian Pines, Kennedy Space center and Pavia University datasets, respectively. However, the spatial features were not extracted in 3D. Also, in future transfer learning could help to extend samples and improve accuracy.

Resource-frugal quantized spectral CNN was employed by [64]. It used a small format, such binary or integer numbers, to express the weights and activations. The deep model was initially trained with full precision, followed by false quantization, training, and final low-bit quantization. As a transitional phase, fake quantization was utilised to mimic the quantization of weights and activations. Salinas Valley and Pavia University were the subjects of the experiment. This model, which was four times smaller than its original competitors, segregated the market just as well. The memory footprint of the large-capacity variant was lessened as a result. Changing the quantization levels might make it easier to comprehend the capabilities of the deep learning model.

Vaddi and Manoharan [85] worked on data normalization and CNN based classification of HSI. The normalization was performed by dividing the scalar pixel values with the maximum pixel intensity value. Probabilistic PCA extracted the spectral features while Gabor filter acquired the spatial features. The experiment was performed on Indian Pines, Salinas valley and Pavia University dataset where the proposed approach gave highest accuracy as compared to other state of art approaches. The experiment's steps are highlighted in Fig. 28

Various deep neural network models were used by [43] for HSI analysis. In first approach, multi scale spatial features were extracted using convolution network based on VGG-verydeep-16. The deep scale spatial features were fused with spectral features using weighted fusion method and z-score. It was used to segment the scenes and obtained pixel based classification results on Indian Pines dataset. In second approach, the authors used Recursive Autoencoders (RAE). It formed high level spatial spectral features from the original data. The spatial features of the pixel were learned using weighting scheme based on the neighbouring pixels. The weights were determined using the spectral similarity between the investigated pixel and neighbouring pixels. Unsupervised RAE was employed on Pavia University dataset achieving an accuracy of 99.91%. Third approach involved Superpixels based Multi Local CNN (SML-CNN). Superpixels were formed using a SLIC algorithm. Multiple local regions of superpixels were jointly represented to get different semantic environment of each superpixel, even if there was spectral similarity. Features were fused from the same. The technique achieved a good accuracy.

To identify and segment the peanuts as healthy, moldy and damaged [55] developed Hypernet, Unet, Deeplab v3+ and Segnet. These were used as control model for comparison. The features were pre-extracted and enhanced which improved the models average accuracy by 1.15% and 4.96%, respectively. However, hypernet had the highest accuracy of 92.07%.

HSI analysis of ripeness of strawberry was examined by [29] in field and laboratory conditions using AlexNet CNN. Specific wavelengths shortlisted using Sequential Feature

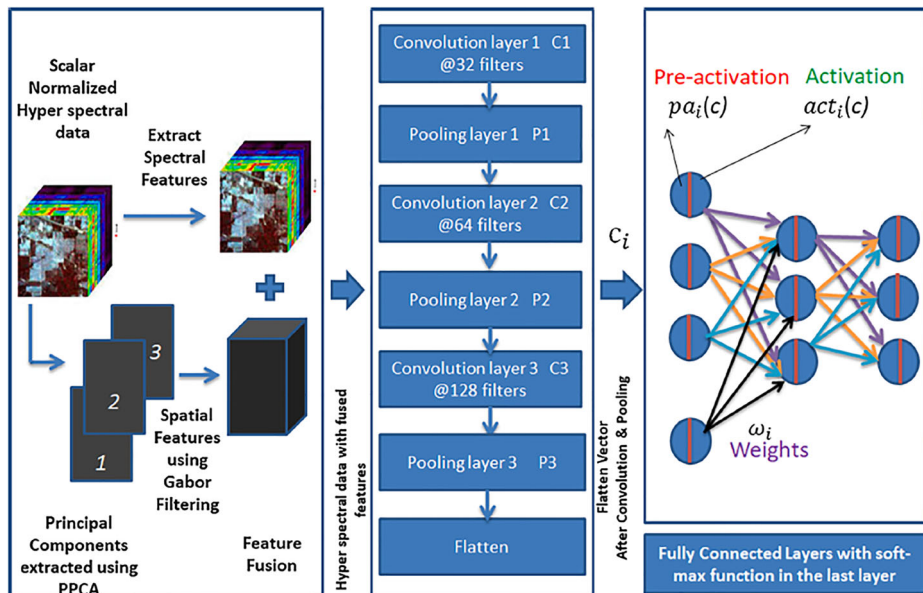


**Fig. 28** Steps used in HSI segmentation and classification [85]

Selection (SFS) gave spectral features. Using these spectral features, spatial information was obtained using PCA. The technique recorded an accuracy of 98.6%. The huge success of AlexNet is attributed to its ability to handle large number of parameters and it can also leverage GPU for training the data.

Traditional deep learning models caused information loss while representing hyperspectral pixels. Hence, [62] considered HSI data as sequential data and applied Recurrent Neural Network (RNN). It used parametric rectified tanh (PRetanh) activation function. This function used high learning rates and did not diverge while training the samples. To construct recurrent layer in network, modified gated recurrent unit was adopted. It has statistically better performance than CNN and SVM-RBF on Indian Pines and Pavia University.

In earlier works of RNN, whole of the spectral bands have been considered which does not explore the spectral sequence properties well. Hang et al. [37] used cascaded RNN to explore the complementary and redundant information of HSIs. Two strategies were built to learn distinct features. In first, weighted fusion of features from both the layers was carried out. In second approach, weighted combination of various loss functions from both the layers was done. Spatial features were captured from each band, few convolutional layers were embedded. It recorded highest OA of 91.79% on Indian Pines and 90.30% on Pavia University.

Lu et al. [56] performed semantic road segmentation in urban and rural areas. Fully Convolutional Network (FCN), Unet were trained and evaluated. For each of these models, MobileNet, DenseNet and ResNet were used as feature encoders. Intersection over Union was the evaluation metric for road area only. The complexity of the models in terms of volumes of parameters involved did not affect the mIoU, where mIoU is the average IoU of the road area in every scene. Unet with ResNet and MobileNet were quite close in performance where the former and latter had mIoU values of 0.9247 and 0.9220, respectively. The

**Table 8** Comparison analysis of deep learning based segmentation

Authors	Methodology used	Evaluation parameters
Zabalza et al. [97]	Stacked Segmented Autoencoders	• IP: OA-80.66%. • PU: OA-97.5%.
Li et al. [50]	Deep convolutional neural network, PCA, GLCM, ELM.	• IP: OA-98.08%, AA-97.67% and k-97.81%. • PU : OA-96.46%, AA-93.32% and k-95.31%.
Pan et al. [66]	Multi-grained network called MugNet, Spectral MugNet, Spatial MugNet, SVM classification	• IP: OA-90.65%. • OA of 90.82% and 93.15% on Grss_dfc_2013 and Grss_dfc_2014 datasets.
Paoletti et al. [67]	3D CNN	• IP: OA-98.37%, AA-99.27% and k-98.15%. • PU: OA-98.06%, AA-98.61% and k-97.44%.
Chen et al. [18]	Adaptive spatial window, Spectral features extraction, Features merge with convolutional layer.	• IP: OA-98.02%. • On combination with SVM, highest accuracy of 98.39% and 98.44% was obtained in the IP and PU dataset.
Cheng et al. [22]	Off the shelf CNN models, Metric learning framework	• IP: OA-98.9%, k-0.987. • PU: OA-99.34%, k-0.991. • Sa: OA-99.58%, k-0.995.
Zhou et al. [103]	Spectral-spatial LSTM, PCA.	Improved the classification accuracy by at least 2.69%, 1.53% and 1.08% on Indian Pines, Pavia University and Kennedy Space Centre datasets, respectively.
Cao and Guo [9]	3D-2D SSHDR	• IP : OA-99.46%, AA-99.43% and k-99.38%. • KSC : OA-99.89%, AA-99.77% and k-99.88%. • PU : OA-99.81%, AA-99.69% and k-99.74%.
Nalepa et al. [64]	Resource frugal quantized spectral CNN	The model four times smaller in size than original counterparts, segmented equally well.
Vaddi and Manoharan [85]	CNN, Probabilistic PCA, Gabor Filter	• IP : OA-99.02% and AA-99.17%. • PU : OA-99.94% and AA-99.92%.
Jiao et al. [43]	VGG-verydeep-16 network, RAEs, Superpixels using SLIC	Accuracy of 99.91% on PU using RAEs.

comparative analysis of various Deep Learning segmentation techniques has been discussed in Table 8.

## 4 Discussion

After extensive survey of segmentation aided classification of HSI, following insights have been observed.

- In this study it has been found that **thresholding** based segmentation is majorly used to extract ROI and form binary mask in HSI images of fruits. The highest OA recorded is 99.90% along with RF classifier. The ease of use of this strategy is its main benefit.

- Adaptive threshold for remotely sensed image gives mixed results in classification map. This method is quite theoretical, as it could also apply to remotely detected images where one pixel could reflect mixed classes and data imbalance. Optimal thresholding could be tuned to produce clear class labels in order to obtain superior outcomes..
- The authors have commonly used fuzzy c-means and k-means **clustering** to perform segmentation on brain images which includes local spatial information. Along with mentioned methods, density based clustering is also used to segment HSI for land cover classification. The highest OA recorded for the land cover segmentation and classification is as high as 91% using projected and k-means clustering. Some authors have used k-means in testing phase to improve the results of segmentation of decay in potatoes images. The benefit of clustering is using region adjacency properties which extracts spatial features in a better way. But the performance of this approach is sensitive to manual selection of parameters like initial cluster centers, number of clusters and constant distance cutoff. This approach is computationally extensive as well.
  - To detect the contours in the image, extract spectral -spatial and textural information of the remotely sensed land cover dataset, **watershed** approach has been used frequently. Using this approach, highest OA of 99% has been recorded where both pixel-wise and object-wise information has been utilised. A certain amount of research has also been conducted for segmentation of decay on fruits using watershed. In this the authors have usually used morphological gradient images. The major drawbacks of this approach are over-segmentation and sensitivity to noise, which needs further research for improvement in segmentation.
  - For extracting shape based and geometrical properties, **morphological segmentation** has been used for remote sensing dataset. In this, repetitive opening and closing operations are performed on informative bands to reduce salt and pepper noise. Some authors have used different shapes and sizes of SE for better use of spatial properties. With the advantage of using different shapes of SEs, highest OA of 99.82% has been recorded. Peers also used morphological operations before watershed for improved gradient images. Mathematical morphology has also been employed in medical field of HSI analysis for lung cancer identification. Here, it has been used as post processing step to remove gaps between objects and refined the segmentation results.
  - **Edge preserving** based segmentation is usually based on discontinuities in the image via texture, color, contrast and brightness. This helps in preserving useful spatial features in remotely sensed land cover dataset. Edge based filters at different scales have improved the classification results by achieving OA of 99.53%. However, the performance of this approach is sensitive to noise. Few authors have used different degrees of smoothing and blur for extracting spatial features at different scales but these parameters for the same have been chosen manually.
  - **Region growing and merging** approaches have used by authors to group the pixels together on the basis of some homogeneity criteria. While majority of authors have used this approach on remote sensing images, few authors applied it to separate infected kernels of peanuts. Highest OA of 99.71% has been recorded for land cover images that uses spectral spatial correlation and region growing. The requirements for this approach are initial seed points and stopping criteria.
  - The **superpixels** have been usually generated using SLIC or ERS algorithms for segmentation of scenes in land cover images. The spatial features achieved using this approach helps in improving the identification. The superpixels created using SLIC in deep network achieved higher OA of 99.8%. To achieve better spectral spatial features,

**Table 9** Comparison analysis of different segmentation techniques

Technique	Advantages	Disadvantages	Highest value	evaluation parameter's
Thresholding	<ul style="list-style-type: none"> <li>Simplest technique</li> <li>Easier execution as deals with pixel intensities alone</li> </ul>	<ul style="list-style-type: none"> <li>Fixed and Manual Thresholding</li> <li>Worked best to extract and highlight single ROI</li> <li>Does not work with spatial domain</li> <li>Generates salt and pepper noise</li> <li>Good performance on objects with uniform texture</li> <li>Gives mixed results in classification map for land cover</li> </ul>	OA= 99.90% [17]	
Clustering	<ul style="list-style-type: none"> <li>Unsupervised in nature</li> <li>Examines the intrinsic properties of objects to accumulate adjacent and similar pixels.</li> </ul>	<ul style="list-style-type: none"> <li>Highly Computational</li> <li>Difficulty in choosing initial parameters like number of clusters, centroid, distance parameters.</li> <li>Outliers in HSI have not been addressed</li> <li>Clustering not generalised to deal with objects of varying sizes and structures.</li> </ul>	OA= 90% [41]	
Watershed	<ul style="list-style-type: none"> <li>Simple and intuitive</li> <li>Usually provides contours by improving the morphologically reconstructed gradient images.</li> <li>Works well with textured objects.</li> </ul>	<ul style="list-style-type: none"> <li>Does over-segmentation</li> <li>Generates more edges and noise</li> <li>Does not involve both spectral and spatial domains simultaneously</li> </ul>	OA= 99.9% [14]	
Morphological segmentation	<ul style="list-style-type: none"> <li>Powerful spatial features extraction using dilation and erosion operations.</li> <li>Helps improve distorted binary images produced after thresholding</li> </ul>	<ul style="list-style-type: none"> <li>Fixed sizes of Structuring elements</li> <li>Not robust to noisy bands and samples with varying geometrical shapes.</li> </ul>	OA= 99% on PU [57]	

**Table 9** (continued)

Technique	Advantages	Disadvantages	Highest value	evaluation parameter's
Edge Detection based Segmentation	<ul style="list-style-type: none"> <li>• Locates boundaries well in sharp discontinuities among objects.</li> <li>• Improves Signal to Noise ratio.</li> </ul>	<ul style="list-style-type: none"> <li>• Sensitivity to noise in land cover due to varying textures and materials</li> <li>• Better results dependent on smoothing and blur effects applied in advance.</li> <li>• Commonly used Canny edge detector is computational and time consuming.</li> <li>• Spatial irregularities pose a challenge for edge detection.</li> </ul>	OA= 99.5% on PU [87]	
Region based segmentation	<ul style="list-style-type: none"> <li>• Unsupervised in nature.</li> <li>• Region merging can improve over-segmented images especially after watershed segmentation.</li> </ul>	<ul style="list-style-type: none"> <li>• Sensitive to initial seed points chosen as centroids.</li> <li>• Performs better with homogeneous data whereas HSI are highly heterogeneous and imbalanced.</li> <li>• Dependent on manual parameters set for homogeneity functions, for instance threshold for distance computation.</li> </ul>	OA= 99.94% on Sa [4]	
Superpixel segmentation	<ul style="list-style-type: none"> <li>• Carries more contextual information regarding an object than a single pixel.</li> <li>• Compact and Convenient representation of images.</li> </ul>	<ul style="list-style-type: none"> <li>• Computational and time consuming.</li> <li>• Manual selection of scales and number of regions.</li> <li>• The algorithms of 2D images have been implemented on 3D HSI.</li> </ul>	OA= 99.70% [89]	
Deep learning segmentation	<ul style="list-style-type: none"> <li>• No overload of features engineering.</li> <li>• Receives low-level, middle-level and high-level visual representations of images at different layers.</li> <li>• More robust as compared to other learners.</li> </ul>	<ul style="list-style-type: none"> <li>• Needs lots of data for good performance.</li> <li>• Mostly manual hyperparameters have been used.</li> <li>• Over-optimistic accuracy results in HSI due to overlapping data.</li> <li>• computational and time consuming.</li> <li>• No guarantee of performance of deep learning since there no strict rules.</li> </ul>	OA= 99.94% on PU [85]	

few authors have also extracted superpixels at different scales. This approach helps in reducing complexity as learners do not deal with pixel level details but a group of them having similar properties.

- **Deep learning** has been a powerful medium that helps to extract features and segment scenes of land cover dataset. It helps in automatic extraction of spectral and spatial features to improve the results. Using both spectral spatial features and dilated residual networks, OA of 99.46% has been obtained. The reported results are over optimistic due to limited number of training samples.

The advantages and shortcomings of each segmentation technique discussed in the survey have been listed and compared in Table 9. The purpose of the paper is to demonstrate how well traditional segmentation strategies function for HSI. Figure 29 highlights the often used OA of each segmentation technique so that readers may know more about how well each technique performs. In this figure it is obvious that Deep Learning and Watershed have achieved the highest OA of almost 100%. Although, classical techniques have also obtained OA near to 99%, but not on the benchmark datasets. It is interesting to note that the watershed gave such a high OA in the work by [14] where it was combined with deep learning.

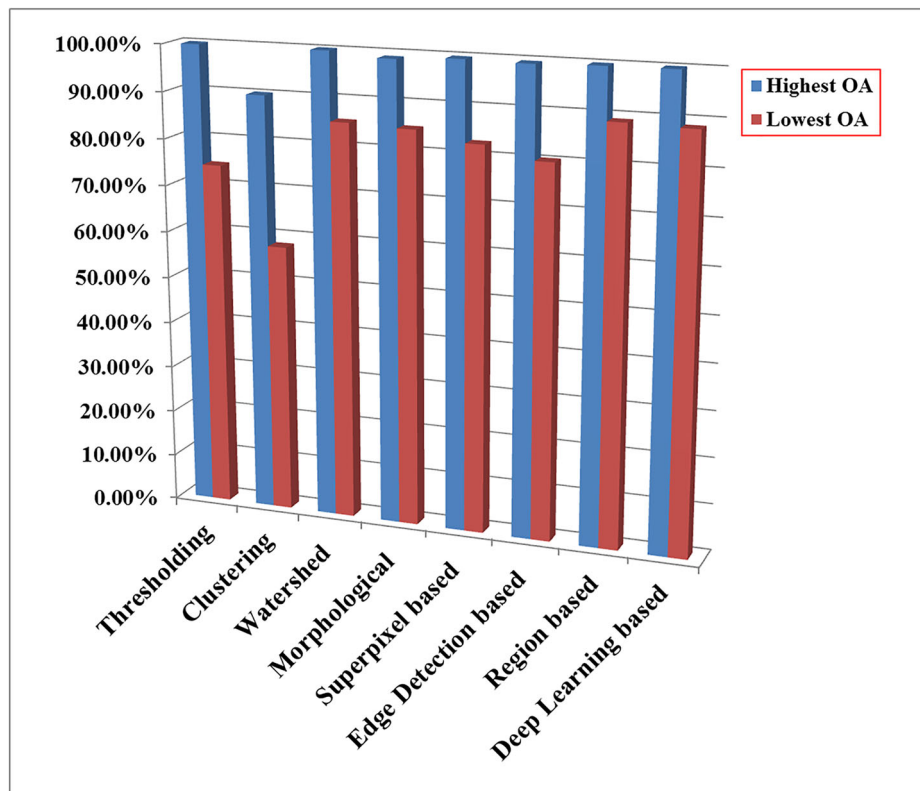


**Fig. 29** The highest and lowest OA achieved by different segmentation techniques in the survey

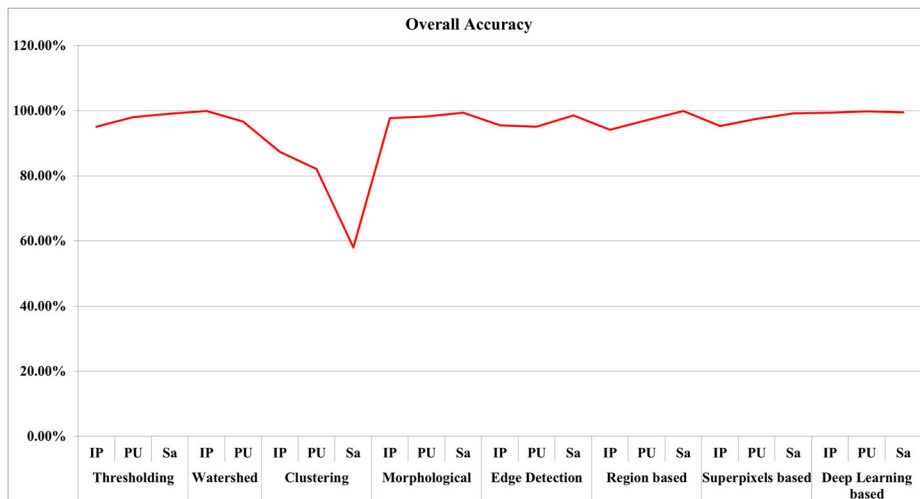


**Fig. 30** OA of segmentation techniques on benchmark datasets

#### 4.1 Performance of segmentation techniques on the benchmark datasets

A general overview of how different segmentation algorithms performed on some of the most widely used land cover datasets is shown in Fig. 30. It is undeniably true that HSI analysis driven by deep learning produces the best OA across all three datasets. Salinas Valley has also scored the greatest OA for methods including morphological, edge detection, and superpixel-based segmentation.

#### 4.2 Experimental analysis

A lot of research and focus is subjected towards the classification techniques on HSI. As the title of the paper suggests, the objective of this paper is to enlighten the readers about existing segmentation techniques also. Some recent papers were analyzed and implemented on our machine to compare the performance in same environment on benchmark dataset namely, Indian Pines(IP) and Pavia University(PU). Traditional machine learning advises against reaching 100% training accuracy as the models might be overfitting. However, recent deep learning trends point to the contrary. Several deep learning models can indeed fit random data with 100% accuracy. It is still an open question to understand the generalization ability of these models. Half of the papers implemented and compared are driven by deep learning in the backend.

Challa et al. [14] segmented the scenes using deep learning and watershed classifier in a very unique manner. With respect to 10% training samples, the OA, AA have been recorded for the comparison. Implemented a paper proposed by Zou et al. [105] on Spatial-spectral exploration for HSI via fusion of convolution networks (SSFCN). The traditional CNN methods are limited by insufficient training samples, hence over optimistic results are obtained due to training-testing leakage. In the implemented paper, better data split techniques and fusion of 3D CNN with 1D CNN is used to tackle the aforementioned concern. In the work by Cao et al. [11] cascaded SVMs (CSVM) were applied on superpixels to obtain better spectral spatial features.

**Table 10** Comparison analysis of different techniques on IP

Class	Train	Test	ConvTW	SSFCN	CSVM	SF-SP-MK
1	4	42	99.50%	40.40%	99.90%	96.20%
2	142	1286	97.62%	77.89%	97.55%	97.10%
3	83	747	99.50%	60.74%	98.75%	97.31%
4	23	214	99.34%	61.80%	97.86%	98.78%
5	48	435	96.78%	67.50%	98.23%	99.9%
6	73	657	98.97%	91.95%	98.61%	99.9%
7	2	26	99.35%	20.14%	99.81%	98.11%
8	47	431	99.90%	81.71%	99.88%	97.71%
9	2	18	99.13%	31.67%	80.00%	91.45%
10	97	875	98.75%	78.15%	96.09%	97.75%
11	245	2210	98.61%	69.32%	97.86%	98.66%
12	59	534	98.89%	40.81%	89.88%	98.65%
13	20	185	99.55%	93.43%	99.99%	99.15%
14	126	1139	99.91%	91.77%	98.25%	98.76%
15	38	348	99.75%	37.93%	96.79%	97.55%
16	9	84	97.54%	75.19%	58.06%	95.65%

The steps for conducting experiment on the above stated papers included the following specifications:

- 10% of samples of each class were taken for training leaving a majority of samples for testing.
- The experiments were conducted on Indian Pines and Pavia University dataset to capture the difference in performance clearly.
- The performance of different techniques have been compared by measuring their accuracy in identifying different classes.
- The comparison among performances of aforementioned techniques have been shown in Tables 10 and 11, Figs. 31 and 32.

**Table 11** Comparison analysis of different techniques on PU

Class	Train	Test	ConvTW	SSFCN	CSVM	SF-SP-MK
1	4	42	99.50%	96.40%	96.90%	98.56%
2	142	1286	99.62%	89.89%	98.55%	98.10%
3	83	747	98.50%	57.74%	97.75%	98.31%
4	23	214	98.34%	83.80%	98.86%	96.78%
5	48	435	98.78%	93.50%	97.76%	98.9%
6	73	657	98.97%	23.95%	96.61%	99.9%
7	2	26	99.35%	60.14%	97.81%	99.11%
8	47	431	98.90%	87.71%	98.88%	98.71%
9	2	18	99.13%	86.67%	99.00%	97.45%

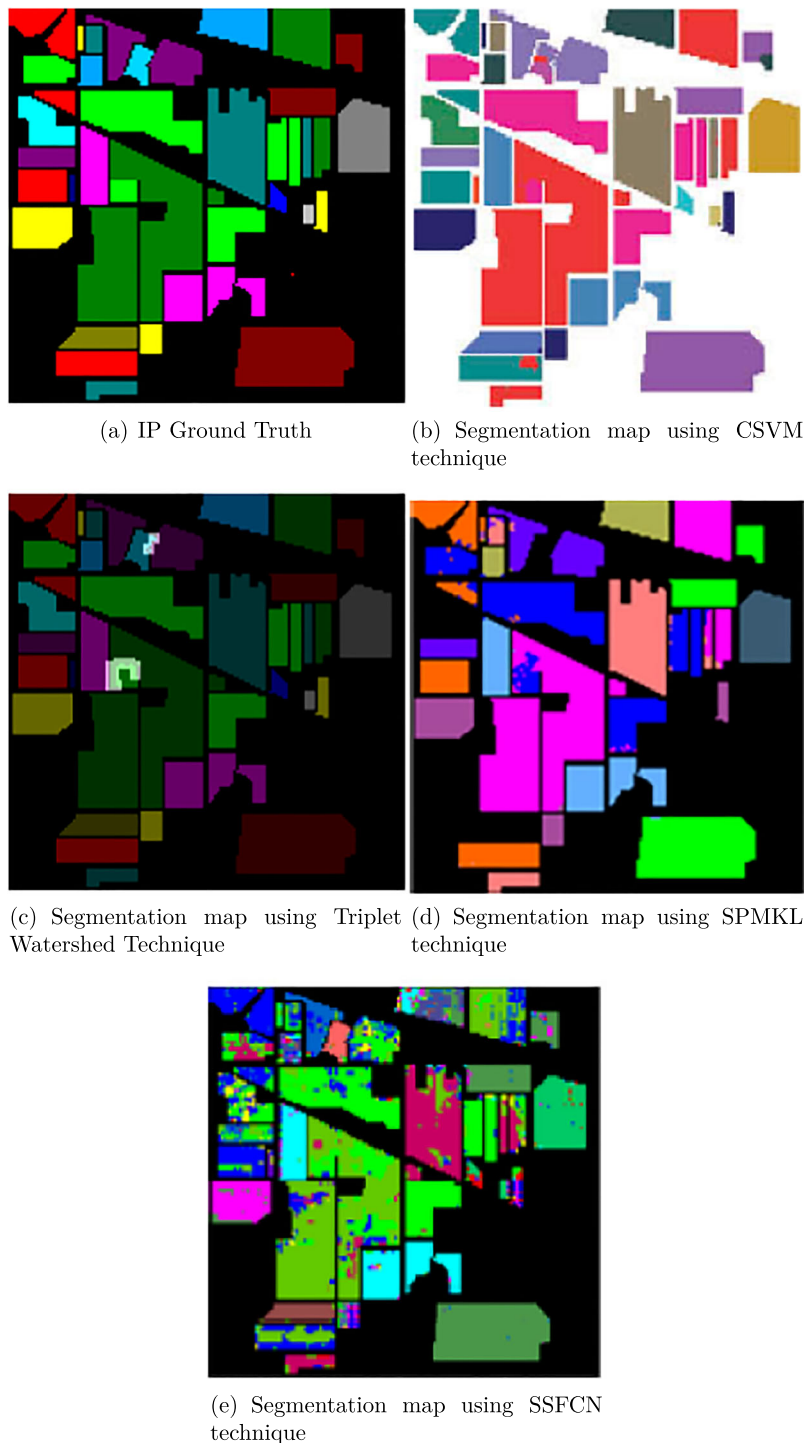
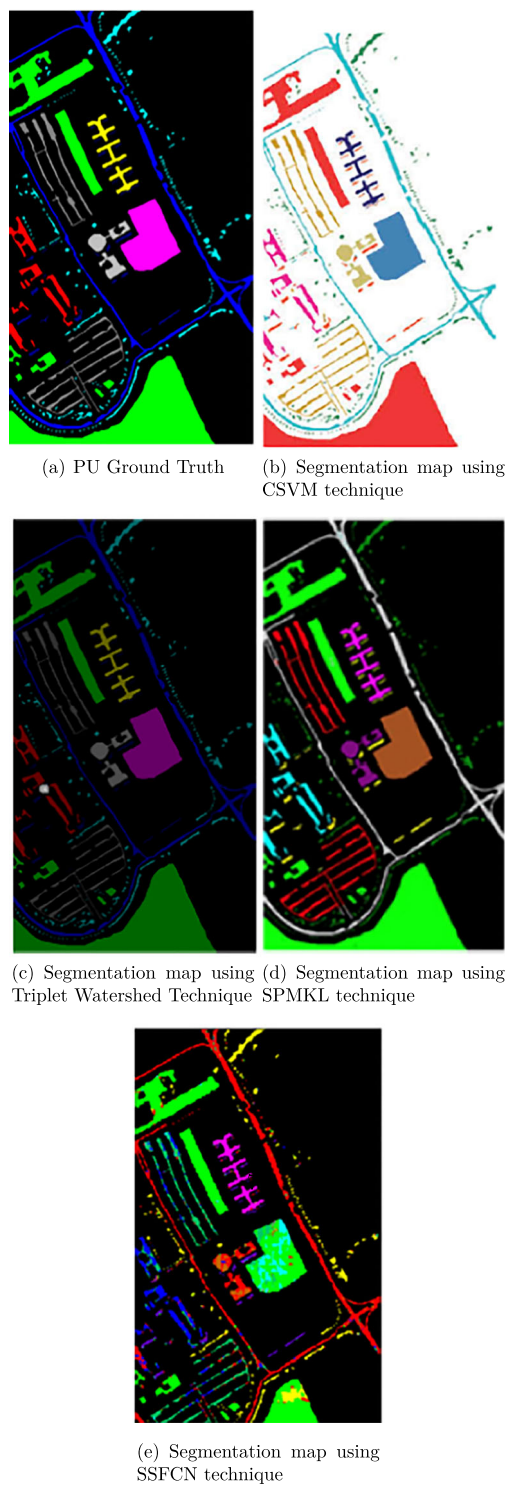


**Fig. 31** Comparison among results of different segmentation techniques on IP, adapted from literature

**Fig. 32** Comparison among results of different segmentation techniques on PU, adapted from literature



## 5 Conclusion and future scope

### 5.1 Conclusion

Research in HSI is evolving and contribution in better identification of objects is needed. With applications in various fields, efficient segmentation is of utmost importance to highlight prominent objects and improve classification results.

The various challenges observed while handling HSI segmentation are listed below:

- **High Dimensionality** - As stated earlier, the hyperspectral images have hundreds of narrow bands which cover the visible to infrared region of electromagnetic spectrum. To handle so many different channels and apply image processing tasks is very complex. The survey highlights the researchers resorting to dimension reduction which is an added effort for segmentation and classification of HSI.
- **Limited Training samples** - The performance of segmentation and classification especially by the deep learning models was extremely over optimistic. This was due to the overlap of training and testing samples.
- **Hughes Phenomenon** - The aforementioned challenges together form a new hurdle for HSI segmentation. It is Hughes phenomenon also called Curse of Dimensionality. Initially, when spectral bands are increased, the accuracy increases but then drastically reduces with further increase in bands.
- **Mixed Pixels** - A few images suffer from spatial dissimilarities and poor resolution. The pixels especially at the boundaries are poorly defined and mixed in nature. By mixed, it is meant that a single pixel contains spectral intensities of various objects. Due to poor spatial definitions, the objects having same spectral value are often segmented or classified into separate classes.
- **Unlabeled Samples** - In the case of land cover images, there are many samples which have not been assigned any label but are present in the scenery. These have been usually left out by the researchers. A few authors have performed hit and trial by merging the unknown samples with the known samples on the basis of spatial adjacency.

This paper reviews the different techniques which have been broadly categorised according to various approaches like thresholding, clustering, watershed and deep learning based methods. A few authors have collected their own HSI images of fruits and vegetables. Many authors used the benchmark datasets like Indian Pines, Pavia University and Salinas Valley. These dataset cover multiple classes of land cover like vegetation, roads, shelter and others. Thresholding is one of the simplest approaches where either fixed threshold, multi-level threshold or adaptive thresholds have been used. It obtained best results using fixed threshold to pop out distinct ROIs whereas clustering has been used extensively to extract several homogeneous partitions of image. Watershed, edge detection and morphological based methods extracted contours, structural and spatial features. To obtain contextual information, pixels are clustered to form superpixels which are further used for processing. Deep learning methods helped in automatic feature extraction, segmentation and classification. Existing segmentation techniques have been implemented on lesser number of training samples which results in over optimistic classification accuracy due to overlapping training and testing samples. The techniques have not considered the possibility of over and under segmentation in their results. Noise removal from various spectral bands has not been considered and more research on textural and semantic features extraction of the objects needs to be performed. The superpixel based segmentation methods have been generated using techniques designed for 2D images and applied on 3D hyperspectral images. Due to this,

spectral-spatial properties are not considered. To deal with limited training samples, transfer learning can be incorporated in future work and improve performance of learners. Also, Meta learning can be explored in future for choosing efficient segmentation methods for HSI.

## 5.2 Future scope

The exhaustive survey brought into light the existing segmentation techniques practiced on HSI, their performance, advantages and drawbacks. Keeping the limitations and challenges of HSI in view, below discussed techniques can put the researchers in a newer and brighter side of HSI analysis.

- **Meta-Learning:** Learning how to learn is the backbone of meta learning. It builds algorithms that learn on how to best combine the predictions of other models and use them on other similar dataset. The potential of Meta learning is untapped research area for HSI segmentation.
- **Some different datasets:** The existing research and more improved techniques need to be tested on newer datasets like Berlin, RIT-18 remote sensory dataset, a road segmentation dataset created by [56]. This will create robust and more generalised techniques for segmentation.
- **Thresholding:** has not been explored more for land cover segmentation. As evident from the survey, thresholding has been majorly performed using manual setups and for binary classification.
- **Extreme Learning Machine (ELM):** ELM is new area to be explored for HSI which deals better with overfitting and slow training speed.
- **Exploring automatic selection and optimization of parameters for thresholding, clustering and other techniques** need an efficient evolutionary approach or Genetic algorithms as it is still an open area for research with scope of lot of improvement.

**Data Availability** Data sharing not applicable to this article as no datasets were generated or analyzed during the current study.

## Declarations

**Conflict of Interests** The authors declare that there is no conflicts of interest.

## References

1. Akbari D (2020a) Improving spatial-spectral classification of hyperspectral imagery by using extended minimum spanning forest algorithm. *Can J Remote Sens* 46(2):146–153
2. Akbari D (2020b) A novel method for spectral-spatial classification of hyperspectral images with a high spatial resolution. *Arab J Geosci* 13(23):1–10
3. Angulo J, Velasco-Forero S, Chanussot J (2009) Multiscale stochastic watershed for unsupervised hyperspectral image segmentation. In: 2009 IEEE international geoscience and remote sensing symposium, vol 3, IEEE, pp III–93
4. Appice A, Malerba D (2019) Segmentation-aided classification of hyperspectral data using spatial dependency of spectral bands. *ISPRS J Photogramm Remote Sens* 147:215–231
5. Azimpour P, Shad R, Ghaemi M, Etemadfarid H (2020) Hyperspectral image clustering with albedo recovery fuzzy c-means. *Int J Remote Sens* 41(16):6117–6134
6. Beirami BA, Mokhtarzade M (2020) Band grouping superpca for feature extraction and extended morphological profile production from hyperspectral images. *IEEE Geosci Remote Sens Lett* 17(11):1953–1957

7. Benediktsson JA, Palmason JA, Sveinsson JR (2005) Classification of hyperspectral data from urban areas based on extended morphological profiles. *IEEE Trans Geosci Remote Sens* 43(3):480–491
8. Binge C, Faxi Z, Xiudan M, Yanan W (2016) Hyperspectral image classification based on image segmentation. In: 2016 international conference on intelligent transportation, big data & Smart City (ICITBS), IEEE, pp 101–104
9. Cao F, Guo W (2020) Deep hybrid dilated residual networks for hyperspectral image classification. *Neurocomputing* 384:170–181
10. Cao X, Lu H, Ren M, Jiao L (2019) Non-overlapping classification of hyperspectral imagery with superpixel segmentation. *Appl Soft Comput* 83:105630
11. Cao X, Wang D, Wang X, Zhao J, Jiao L (2020) Hyperspectral imagery classification with cascaded support vector machines and multi-scale superpixel segmentation. *Int J Remote Sens* 41(12):4530–4550
12. Cariou C, Chehdi K, Le Moan S (2020) Improved nearest neighbor density-based clustering techniques with application to hyperspectral images. In: ICASSP 2020–2020 IEEE international conference on acoustics, speech and signal processing (ICASSP), IEEE, pp 4127–4131
13. Castaings T, Waske B, Atli Benediktsson J, Chanussot J (2010) On the influence of feature reduction for the classification of hyperspectral images based on the extended morphological profile. *Int J Remote Sens* 31(22):5921–5939
14. Challal A, Danda S, Sagar B, Najman L (2021) Triplet-watershed for hyperspectral image classification. arXiv:[2103.09384](https://arxiv.org/abs/2103.09384)
15. Chan T-H, Jia K, Gao S, Lu J, Zeng Z, Ma Y (2015) Pcanet: A simple deep learning baseline for image classification? *IEEE Trans Image Process* 24(12):5017–5032
16. Chauhan NS (2019) Introduction to image segmentation with k-means clustering. <https://www.kdnuggets.com/2019/08/introduction-image-segmentation-k-means-clustering.html>, Accessed December 2021
17. Che W, Sun L, Zhang Q, Tan W, Ye D, Zhang D, Liu Y (2018) Pixel based bruise region extraction of apple using vis-nir hyperspectral imaging. *Comput Electron Agric* 146:12–21
18. Chen C, Jiang F, Yang C, Rho S, Shen W, Liu S, Liu Z (2018a) Hyperspectral classification based on spectral-spatial convolutional neural networks. *Eng Appl Artif Intell* 68:165–171
19. Chen C-W, Tseng Y-S, Mukundan A, Wang H-C (2021) Air pollution: Sensitive detection of pm2. 5 and pm10 concentration using hyperspectral imaging. *Appl Sci* 11(10):4543
20. Chen L, Chen CP, Lu M (2011) A multiple-kernel fuzzy c-means algorithm for image segmentation. *IEEE Transactions on systems, man, and cybernetics, part B (Cybernetics)* 41(5):1263–1274
21. Chen S, Sun T, Yang F, Sun H, Guan Y (2018b) An improved optimum-path forest clustering algorithm for remote sensing image segmentation. *Comput Geosci* 112:38–46
22. Cheng G, Li Z, Han J, Yao X, Guo L (2018) Exploring hierarchical convolutional features for hyperspectral image classification. *IEEE Trans Geosci Remote Sens* 56(11):6712–6722
23. Chu X, Wang W, Ni X, Li C, Li Y (2020) Classifying maize kernels naturally infected by fungi using near-infrared hyperspectral imaging. *Infrared Phys Technol* 105:103242
24. Cui B, Ma X, Xie X, Ren G, Ma Y (2017) Classification of visible and infrared hyperspectral images based on image segmentation and edge-preserving filtering. *Infrared Phys Technol* 81:79–88
25. Das A, Bhardwaj K, Patra S, Bruzzone L (2020) A novel threshold detection technique for the automatic construction of attribute profiles in hyperspectral images. *IEEE journal of selected topics in applied earth observations and remote sensing* 13:1374–1384
26. Dutta T, Dey S, Bhattacharyya S (2020) Automatic clustering of hyperspectral images using qutrit based particle swarm optimization. In: Intelligence enabled research, Springer, pp 21–31
27. Fei B (2020) Hyperspectral imaging in medical applications. In: Data handling in science and technology, vol 32, Elsevier, pp 523–565
28. Gao Y, Cheng T, Wang B (2020a) Nonlinear anomaly detection based on spectral-spatial composite kernel for hyperspectral images. *IEEE geoscience and remote sensing letters*
29. Gao Z, Shao Y, Xuan G, Wang Y, Liu Y, Han X (2020b) Real-time hyperspectral imaging for the in-field estimation of strawberry ripeness with deep learning. *Comput Geosci* 4:31–38
30. Ghamisi P, Benediktsson JA, Ulfarsson MO (2013a) Spectral–spatial classification of hyperspectral images based on hidden markov random fields. *IEEE Trans Geosci Remote Sens* 52(5):2565–2574
31. Ghamisi P, Couceiro MS, Benediktsson JA, Ferreira NM (2012) An efficient method for segmentation of images based on fractional calculus and natural selection. *Expert Syst Appl* 39(16):12407–12417
32. Ghamisi P, Couceiro MS, Martins FM, Benediktsson JA (2013b) Multilevel image segmentation based on fractional-order darwinian particle swarm optimization. *IEEE Transactions on Geoscience and Remote sensing* 52(5):2382–2394
33. Glomb P, Romaszewski M, Cholewa M, Domino K (2018) Application of hyperspectral imaging and machine learning methods for the detection of gunshot residue patterns. *Forensic Sci Int* 290:227–237

34. Gonzalez R (2009) Digital Image Processing. Pearson Education
35. Gu Y, Liu H (2016) Sample-screening mkl method via boosting strategy for hyperspectral image classification. *Neurocomputing* 173:1630–1639
36. Guo Y, Han S, Li Y, Zhang C, Bai Y (2018) K-nearest neighbor combined with guided filter for hyperspectral image classification. *Procedia Comput Sci* 129:159–165
37. Hang R, Liu Q, Hong D, Ghamisi P (2019) Cascaded recurrent neural networks for hyperspectral image classification. *IEEE Trans Geosci Remote Sens* 57(8):5384–5394
38. Hu L, Qi C, Wang Q (2018) Spectral-spatial hyperspectral image classification based on mathematical morphology post-processing. *Procedia Comput Sci* 129:93–97
39. Ismail M, Orlandić M (2020) Segment-based clustering of hyperspectral images using tree-based data partitioning structures. *Algorithms* 13(12):330
40. Ji Y, Sun L, Li Y, Li J, Liu S, Xie X, Xu Y (2019a) Non-destructive classification of defective potatoes based on hyperspectral imaging and support vector machine. *Infrared Phys Technol* 99:71–79
41. Ji Y, Sun L, Li Y, Ye D (2019b) Detection of bruised potatoes using hyperspectral imaging technique based on discrete wavelet transform. *Infrared Phys Technol* 103:103054
42. Jianxin Z, Kangping Z, Junkai W, Xudong H (2020) Color segmentation and extraction of yarn-dyed fabric based on a hyperspectral imaging system. *Textile Research Journal*, pp 0040517520957401
43. Jiao L, Shang R, Liu F, Zhang W (2020) Brain and Nature-inspired Learning, Computation and Recognition. Elsevier
44. Kang X, Duan P, Li S (2020) Hyperspectral image visualization with edge-preserving filtering and principal component analysis. *Inform Fusion* 57:130–143
45. Kumar B, Dikshit O (2017) Hyperspectral image classification based on morphological profiles and decision fusion. *Int J Remote Sens* 38(20):5830–5854
46. Li J, Chen L, Huang W (2018a) Detection of early bruises on peaches (*amygdalus persica l.*) using hyperspectral imaging coupled with improved watershed segmentation algorithm. *Postharvest Biol Technol* 135:104–113
47. Li J, Luo W, Wang Z, Fan S (2019a) Early detection of decay on apples using hyperspectral reflectance imaging combining both principal component analysis and improved watershed segmentation method. *Postharvest Biol Technol* 149:235–246
48. Li J, Zhang R, Li J, Wang Z, Zhang H, Zhan B, Jiang Y (2019b) Detection of early decayed oranges based on multispectral principal component image combining both bi-dimensional empirical mode decomposition and watershed segmentation method. *Postharvest Biol Technol* 158:110986
49. Li X, Li R, Wang M, Liu Y, Zhang B, Zhou J (2018b) Hyperspectral imaging and their applications in the nondestructive quality assessment of fruits and vegetables. In: Hyperspectral imaging in agriculture, food and environment. IntechOpen Limited London, UK, pp 27–63
50. Li Y, Xie W, Li H (2017) Hyperspectral image reconstruction by deep convolutional neural network for classification. *Pattern Recogn* 63:371–383
51. Lima C, Correa L, Byrne H, Zezell D (2018) K-means and hierarchical cluster analysis as segmentation algorithms of fir hyperspectral images collected from cutaneous tissue. In: 2018 SBFoton international optics and photonics conference (SBFoton IOPC), IEEE, pp 1–4
52. Lin L, Zhang S (2020) Superpixel segmentation of hyperspectral images based on entropy and mutual information. *Appl Sci* 10(4):1261
53. Lin Z, Chen Y, Zhao X, Wang G (2013) Spectral-spatial classification of hyperspectral image using autoencoders. In: 2013 9th international conference on information, communications & signal processing, IEEE, pp 1–5
54. Liu Y, Cao G, Sun Q, Siegel M (2015) Hyperspectral classification via deep networks and superpixel segmentation. *Int J Remote Sens* 36(13):3459–3482
55. Liu Z, Jiang J, Qiao X, Qi X, Pan Y, Pan X (2020) Using convolution neural network and hyperspectral image to identify moldy peanut kernels. *LWT* 132:109815
56. Lu J, Liu H, Yao Y, Tao S, Tang Z, Lu J (2020) Hsi road: a hyper spectral image dataset for road segmentation. In: 2020 IEEE international conference on multimedia and expo (ICME), IEEE, pp 1–6
57. Lu Q, Hu X (2020) Hyperspectral image classification via exploring spectral-spatial information of saliency profiles. *IEEE Journal of selected topics in applied earth observations and remote sensing* 13:3291–3303
58. Lv ZY, Zhang P, Benediktsson JA, Shi WZ (2014) Morphological profiles based on differently shaped structuring elements for classification of images with very high spatial resolution. *IEEE Journal of selected topics in applied earth observations and remote sensing* 7(12):4644–4652
59. Mehta A, Dikshit O (2016) Projected clustering of hyperspectral imagery using region merging. *Remote Sens Lett* 7(8):721–730

60. Mehta A, Dikshit O (2017) Segmentation-based clustering of hyperspectral images using local band selection. *J Appl Remote Sens* 11(1):015028
61. Minaee S, Boykov YY, Porikli F, Plaza AJ, Kehtarnavaz N, Terzopoulos D (2021) Image segmentation using deep learning: A survey. *IEEE Transactions on pattern analysis and machine intelligence*
62. Mou L, Ghamisi P, Zhu XX (2017) Deep recurrent neural networks for hyperspectral image classification. *IEEE Trans Geosci Remote Sens* 55(7):3639–3655
63. Myasnikov EV (2017) Hyperspectral image segmentation using dimensionality reduction and classical segmentation approaches. 41(4)
64. Nalepa J, Antoniak M, Myller M, Lorenzo PR, Marcinkiewicz M (2020) Towards resource-frugal deep convolutional neural networks for hyperspectral image segmentation. *Micropress Microsyst* 73:102994
65. Noviyanto A, Abdulla WH (2019) Segmentation and calibration of hyperspectral imaging for honey analysis. *Comput Electron Agric* 159:129–139
66. Pan B, Shi Z, Xu X (2018) Mugnet: Deep learning for hyperspectral image classification using limited samples. *ISPRS J Photogramm Remote Sens* 145:108–119
67. Paoletti M, Haut J, Plaza J, Plaza A (2018) A new deep convolutional neural network for fast hyperspectral image classification. *ISPRS J Photogramm Remote Sens* 145:120–147
68. Peter Protzel AL (2015) Superpixels and their application for visual place recognition in changing environments. <https://nbn-resolving.org/urn:nbn:de:bsz:ch1-qucosa-190241>, Accessed December 2021
69. Pisani RJ, Nakamura RYM, Riedel PS, Zimback CRL, Falcao AX, Papa JP (2014) Toward satellite-based land cover classification through optimum-path forest. *IEEE Trans Geosci Remote Sens* 52(10):6075–6085
70. Qiao X, Jiang J, Qi X, Guo H, Yuan D (2017) Utilization of spectral-spatial characteristics in shortwave infrared hyperspectral images to classify and identify fungi-contaminated peanuts. *Food Chem* 220:393–399
71. Quesada-Barriuso P, Heras DB, Argüello F (2021) Gpu accelerated waterpixel algorithm for superpixel segmentation of hyperspectral images. *The Journal of Supercomputing*, pp 1–13
72. Kulkarni SA, Kamath R (2014) Mri brain image segmentation by edge detection and region selection
73. Song J, Hu M, Wang J, Zhou M, Sun L, Qiu S, Li Q, Sun Z, Wang Y (2019) Alk positive lung cancer identification and targeted drugs evaluation using microscopic hyperspectral imaging technique. *Infrared Phys Technol* 96:267–275
74. Stéfan van der W, Johannes L, Schönberger JN-IFBJDWNYEGTY (2014a) Image manipulation and processing using numpy and scipy. [https://scipy-lectures.org/advanced/image\\_processing/](https://scipy-lectures.org/advanced/image_processing/), Accessed December 2021
75. Stéfan van der W, Johannes L, Schönberger J. N.-I. F. B. J. D. W. N. Y. E. G. T. Y (2014b) Image manipulation and processing using numpy and scipy. [https://scipy-lectures.org/advanced/image\\_processing/](https://scipy-lectures.org/advanced/image_processing/), Accessed December 2021
76. Sudakov I, Essa A, Mander L, Gong M, Kariyawasam T (2017) The geometry of large tundra lakes observed in historical maps and satellite images. *Remote Sens* 9(10):1072
77. Tarabalka Y, Chanussot J, Benediktsson JA (2010a) Segmentation and classification of hyperspectral images using watershed transformation. *Pattern Recogn* 43(7):2367–2379
78. Tarabalka Y, Fauvel M, Chanussot J, Benediktsson JA (2010b) Svm-and mrf-based method for accurate classification of hyperspectral images. *IEEE Geosci Remote Sens Lett* 7(4):736–740
79. Tarabalka Y, Tilton JC (2012) Improved hierarchical optimization-based classification of hyperspectral images using shape analysis. In: 2012 IEEE international geoscience and remote sensing symposium, IEEE, pp 1409–1412
80. Tian X, Fan S, Huang W, Wang Z, Li J (2020) Detection of early decay on citrus using hyperspectral transmittance imaging technology coupled with principal component analysis and improved watershed segmentation algorithms. *Postharvest Biol Technol* 161:111071
81. Tian X, Li J, Wang Q, Fan S, Huang W, Zhao C (2019) A multi-region combined model for non-destructive prediction of soluble solids content in apple, based on brightness grade segmentation of hyperspectral imaging. *Biosystems Eng* 183:110–120
82. Torres I, Sánchez M-T, Cho B-K, Garrido-Varo A, Pérez-marin D (2019) Setting up a methodology to distinguish between green oranges and leaves using hyperspectral imaging. *Comput Electron Agric* 167:105070
83. Torti E, Florimbi G, Castelli F, Ortega S, Fabelo H, Callicó GM, Marrero-Martin M, Leporati F (2018) Parallel k-means clustering for brain cancer detection using hyperspectral images. *Electronics* 7(11):283
84. Tu B, Li N, Fang L, Fei H, He D (2018) Classification of hyperspectral images via weighted spatial correlation representation. *J Vis Commun Image Represent* 56:160–166

85. Vaddi R, Manoharan P (2020) Hyperspectral image classification using cnn with spectral and spatial features integration. *Infrared Phys Technol*, pp 103296
86. Verma H, Agrawal R, Sharan A (2016) An improved intuitionistic fuzzy c-means clustering algorithm incorporating local information for brain image segmentation. *Appl Soft Comput* 46:543–557
87. Wan X, Zhao C (2019) Spectral-spatial hyperspectral image classification combining multi-scale bi-exponential edge-preserving filtering and susan edge detector. *Infrared Phys Technol* 102:103055
88. Wang H, Li W, Huang W, Niu J, Nie K (2020a) Research on land use classification of hyperspectral images based on multiscale superpixels. *Math Biosci Eng* 17(5):5099–5119
89. Wang Y, Yu W, Fang Z (2020b) Multiple kernel-based svm classification of hyperspectral images by combining spectral, spatial, and semantic information. *Remote Sens* 12(1):120
90. Wang Y-J, Jin G, Li L-Q, Liu Y, Kalkhajeh YK, Ning J-M, Zhang Z-Z (2020c) Nir hyperspectral imaging coupled with chemometrics for nondestructive assessment of phosphorus and potassium contents in tea leaves. *Infrared Phys Technol* 108:103365
91. Wu Y, Hu B, Gao X, Wei R (2018) Hyperspectral image classification based on adaptive segmentation. *Optik* 172:612–621
92. Xia J, Bombrun L, Adalı T, Berthoumieu Y, Germain C (2016) Spectral–spatial classification of hyperspectral images using ica and edge-preserving filter via an ensemble strategy. *IEEE Transactions on geoscience and remote sensing* 54(8):4971–4982
93. Ye D, Sun L, Tan W, Che W, Yang M (2018) Detecting and classifying minor bruised potato based on hyperspectral imaging. *Chemometr Intell Lab Syst* 177:129–139
94. Yijie W, CHENG J (2018) Rapid and non-destructive prediction of protein content in peanut varieties using near-infrared hyperspectral imaging method. *Grain & Oil Sci Technol* 1(1):40–43
95. Youn S, Lee C (2013) Edge detection for hyperspectral images using the bhattacharyya distance. In: 2013 international conference on parallel and distributed systems, IEEE, pp 716–719
96. Yu H, Gao L, Liao W, Zhang B, Pižurica A, Philips W (2017) Multiscale superpixel-level subspace-based support vector machines for hyperspectral image classification. *IEEE Geosci Remote Sens Lett* 14(11):2142–2146
97. Zabalza J, Ren J, Zheng J, Zhao H, Qing C, Yang Z, Du P, Marshall S (2016) Novel segmented stacked autoencoder for effective dimensionality reduction and feature extraction in hyperspectral imaging. *Neurocomputing* 185:1–10
98. Zeng S, Wang Z, Huang R, Chen L, Feng D (2019) A study on multi-kernel intuitionistic fuzzy c-means clustering with multiple attributes. *Neurocomputing* 335:59–71
99. Zhang L, Sun H, Rao Z, Ji H (2020) Hyperspectral imaging technology combined with deep forest model to identify frost-damaged rice seeds. *Spectrochimica Acta Part A: Mol Biomol Spectrosc* 229:117973
100. Zhang Y, Kang X, Li S, Duan P, Benediktsson JA (2019a) Feature extraction from hyperspectral images using learned edge structures. *Remote Sensing Lett* 10(3):244–253
101. Zhang Y, Liu K, Dong Y, Wu K, Hu X (2019b) Semisupervised classification based on slic segmentation for hyperspectral image. *IEEE Geosci Remote Sens Lett* 17(8):1440–1444
102. Zhang Y, Wu L, Deng L, Ouyang B (2021) Retrieval of water quality parameters from hyperspectral images using a hybrid feedback deep factorization machine model. *Water Res* 204:117618
103. Zhou F, Hang R, Liu Q, Yuan X (2019a) Hyperspectral image classification using spectral-spatial lstms. *Neurocomputing* 328:39–47
104. Zhou P, Han J, Cheng G, Zhang B (2019b) Learning compact and discriminative stacked autoencoder for hyperspectral image classification. *IEEE Trans Geosci Remote Sens* 57(7):4823–4833
105. Zhou S, Sun L, Xing W, Feng G, Ji Y, Yang J, Liu S (2020) Hyperspectral imaging of beet seed germination prediction. *Infrared Physics & Technology*, pp 103363

**Publisher's note** Springer Nature remains neutral with regard to jurisdictional claims in published maps and institutional affiliations.

Springer Nature or its licensor holds exclusive rights to this article under a publishing agreement with the author(s) or other rightsholder(s); author self-archiving of the accepted manuscript version of this article is solely governed by the terms of such publishing agreement and applicable law.